gels

MDPI

*Article*

# Structure and Photocatalytic Properties of Ni-, Co-, Cu-, and Fe-Doped $TiO_2$ Aerogels

**Tinoco Navarro Lizeth Katherine [1,*], Bednarikova Vendula [1], Kastyl Jaroslav [1] and Cihlar Jaroslav [1,2]**

[1] CEITEC-Central European Institute of Technology, Brno University of Technology, Purkynova 656/123, 612 00 Brno, Czech Republic; vendula.bednarikova@ceitec.vutbr.cz (B.V.); jaroslav.kastyl@tescan.com (K.J.); jaroslav.cihlar@ceitec.vutbr.cz (C.J.)

[2] Institute of Materials Science and Engineering, Brno University of Technology, Technicka 2, 616 69 Brno, Czech Republic

* Correspondence: katherine.tinoco@ceitec.vutbr.cz

**Abstract:** $TiO_2$ aerogels doped with Ni, Co, Cu, and Fe were prepared, and their structure and photocatalytic activity during the decomposition of a model pollutant, acid orange (AO7), were studied. After calcination at 500 °C and 900 °C, the structure and composition of the doped aerogels were evaluated and analyzed. XRD analysis revealed the presence of anatase/brookite and rutile phases in the aerogels along with other oxide phases from the dopants. SEM and TEM microscopy showed the nanostructure of the aerogels, and BET analysis showed their mesoporosity and high specific surface area of 130 to 160 $m^2 \cdot g^{-1}$. SEM–EDS, STEM–EDS, XPS, EPR methods and FTIR analysis evaluated the presence of dopants and their chemical state. The concentration of doped metals in aerogels varied from 1 to 5 wt.%. The photocatalytic activity was evaluated using UV spectrophotometry and photodegradation of the AO7 pollutant. Ni–$TiO_2$ and Cu–$TiO_2$ aerogels calcined at 500 °C showed higher photoactivity coefficients ($k_{aap}$) than aerogels calcined at 900 °C, which were ten times less active due to the transformation of anatase and brookite to the rutile phase and the loss of textural properties of the aerogels.

**Keywords:** aerogels; anatase; brookite; transition metal ions; photocatalytic properties



**Citation:** Lizeth Katherine, T.N.; Vendula, B.; Jaroslav, K.; Jaroslav, C. Structure and Photocatalytic Properties of Ni-, Co-, Cu-, and Fe-Doped $TiO_2$ Aerogels. *Gels* **2023**, *9*, 357. https://doi.org/10.3390/gels9050357

Academic Editors: Miguel Sanchez-Soto, Carlos A. García-González, Luísa Durães and Tobias Abt

Received: 28 February 2023
Revised: 19 April 2023
Accepted: 20 April 2023
Published: 24 April 2023



## 1. Introduction

$TiO_2$ aerogels have promising applications in environmental remediation, especially by photodegradation of pollutants [1,2]. However, their narrow bandgap and high recombination rate of charge carriers ($e^-/h^+$) are issues that need to be addressed [3]. Creating more surfactant sites, heterojunctions, oxygen vacancies or defects can improve the kinetics of redox reactions on the catalyst surface and accelerate the cleavage of H–OH bonds, leading to improved photocatalytic activity [4–6].

Previous studies have shown that biphasic $TiO_2$ of anatase/rutile and anatase/brookite has better visible light photocatalytic activity [7–9], attributed to the delayed charge recombination effect initiated by the electron-hole separation effect. However, design rules are still needed to develop more efficient neutral catalysts [10]. Improving the crystallinity of $TiO_2$ can increase the probability that charge carriers ($e^-/h^+$) reach the photocatalyst surface without being trapped by crystal defects [11], thus preventing their recombination and allowing subsequent redox reactions [12].

Therefore, doping non-metal and metal ions is an effective strategy to tune the band gap by introducing new energy levels between them, which improves the photocatalytic properties of $TiO_2$ [13]. In this regard, cationic dopants served to prolong visible light absorption and enriched the high-temperature stability of the anatase phase of $TiO_2$ [14,15]. Various transition metals such as Fe, Cu, Ni, Cr, and Co have been successfully doped on $TiO_2$ to minimize charge transfer at the interface [16–18]. The scavenger of photogenerated holes in oxidized forms reacts with surface-adsorbed hydroxyl ions to form hydroxyl

radicals and $O_2$ in the $TiO_2$ surface lattice [19–21]. Entrapment experiments have also been studied mainly for the photodegradation of pollutants using various doped $TiO_2$ aerogels [1,22].

Using $Cu^{2+}$ as a $TiO_2$ catalyst dopant showed that the photocatalytic activity of Cu-$TiO_2$ increased in acid orange 7 (AO7) degradation. The reason was that $Cu^{2+}$ acted as an electron scavenger to form $Cu^{+}$, thereby increasing the oxidation of the substrate [2,23]. In addition, cobalt-doped $TiO_2$ [24] has been studied in various oxidation applications, such as the degradation of methylene blue and methyl orange [25,26]. Another study revealed new defect states in anatase-$TiO_2$ and enhanced Ni dopants such as oxygen vacancies [27]. In addition, photoluminescence (PL) studies reported a region of transparency of doped Ni–$TiO_2$ due to an increase in defect density and the transformation of brookite into an amorphous phase. Nickel cations induce the release of carbon and oxygen atoms, resulting in a significant oxygen deficiency [28]. In addition, oxygen vacancies can change the surface properties of $TiO_2$ and affect the adsorption of organic pollutants on its surface. The presence of oxygen vacancies can create surface defects that can provide more active sites for the adsorption of organic pollutants, leading to better photocatalytic activity [29].

Synthesis conditions, dopants, and complexes present in the precursors significantly affect the photoactivity of $TiO_2$ aerogels [16]. Acid-catalyzed sol-gel synthesis is a simple and effective way to prepare stable, mesoporous $TiO_2$ aerogels with a large specific surface area [30,31]. The –COOH and –OH ligand substituents, provided by the organic complexes, offer proper gel networks and photoinduced structures that increase active surface sites and heterojunction defects, thus improving the photocatalytic activity of the material. The optimal formation of crystalline phases depends on the nature of the complexing agent coordinated with the central titanium [32]. Transition metal–organic salts are cheap and easy to handle and release metal complexes in basic suspensions, making them a promising source of dopants for metal-doped $TiO_2$ aerogels [33].

A promising method for synthesizing mesoporous networks of $TiO_2$ aerogels doped with transition metals is sol-gel synthesis using acetate salts as a source of dopants [34,35].

The aim of the research is to evaluate the effect of metal ions nickel ($Ni^{2+}$), cobalt ($Co^{2+}$), copper ($Cu^{2+}$), and iron ($Fe^{3+}$) on the structure and photocatalytic activity of metal-doped $TiO_2$ aerogels prepared by sol-gel acid-catalyzed synthesis of Ti alkoxide in the presence of transition metals acetate salts.

## 2. Results and Discussion

### *2.1. Crystallographic Analysis of Ni, Co, Cu, and Fe-Doped $TiO_2$ Aerogels: Synthesis, Nanostructure, and Calcination Effects*

Figure 1a–c shows a schematic of the synthesis process of metal-doped $TiO_2$ aerogels using Ni, Co, Cu, and Fe precursors. The process involves several steps, starting with the preparation of alcogels, which are then subjected to gel aging and solvent exchange using acetone. The final step involves supercritical drying used to form metal-doped $TiO_2$ aerogels. Prior to supercritical drying, the metal-doped $TiO_2$ aerogels were immersed in acetone. The weak binding of transient ions in the alcohol gel structure caused them to diffuse into the acetone solution, resulting in incomplete retention of $Ni^{2+}$, $Co^{2+}$, $Cu^{2+}$, and $Fe^{3+}$ ions in the mesoporous network of aerogels, as shown in Figure 1b. The presence of these ions in the mesoporous network of aerogels can induce surface defects and increase the surface area of aerogels, increasing its photoactivity. $TiO_2$ aerogels after supercritical drying were amorphous (Figure S1) and not active in photocatalytic tests. During calcination at temperatures of 500 °C and 900 °C, crystalline phases were formed that were photocatalytically active. It was assumed that in particular, calcination at high temperature (900 °C) would lead to the formation of crystalline $TiO_2$ phases doped with Ni, Co, Cu, and Fe.

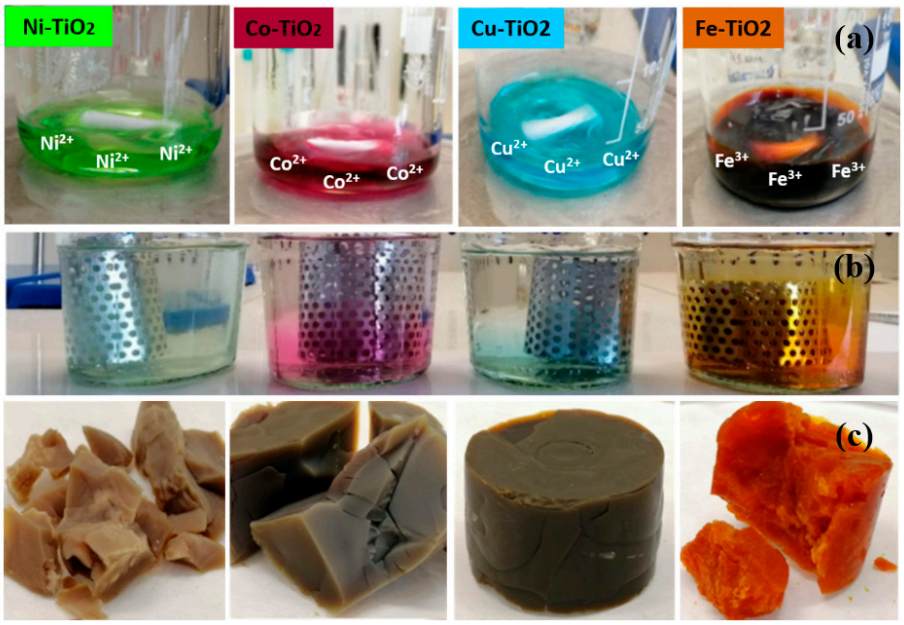


**Figure 1.** (**a**) The process of synthesis of the metal-doped $TiO_2$ aerogels prepared with the metal acetate precursor of $Ni^{2+}$, $Co^{2+}$, $Cu^{2+}$, $Fe^{3+}$ ions. (**b**) Involving the gelation of the alcogels followed by solvent exchange with acetone. (**c**) Finally, supercritical drying to obtain aerogel samples.

$TiO_2$ occurs in studied samples in three primary phases, rutile (tetragonal, P42/mnm), anatase (tetragonal, I41/amd), and brookite (orthorhombic, Pbca). The XRD patterns show anatase (011) and brookite (210) peaks at 25.3° and 25.6°, respectively (Figure 2a). Brookite (211) was found at 30.82° in 2θ for all metal-doped $TiO_2$ aerogel samples calcined at 500 °C [36]. After calcination at 900 °C, all metal-doped aerogels were transformed from anatase to the rutile phase (110) [35]; see Table 1. Ni-$TiO_2$ and Cu-$TiO_2$ aerogel samples calcined at 500 °C contained the most brookite and the least anatase [36], while the undoped $TiO_2$ sample mainly contained anatase and some rutile. At a higher calcination temperature (900 °C), the rutile content increased from 87 to 98 wt.% for all doped aerogels; the undoped sample contained only the rutile phase. The anatase crystallite size was 4–7 nm at 500 °C, less than the undoped $TiO_2$ aerogel. The size of brookite crystallites was in the range of 2–3 nm [37]. At the calcination temperature of 900 °C, the rutile crystallites' size increased to 66–78 nm in all samples.

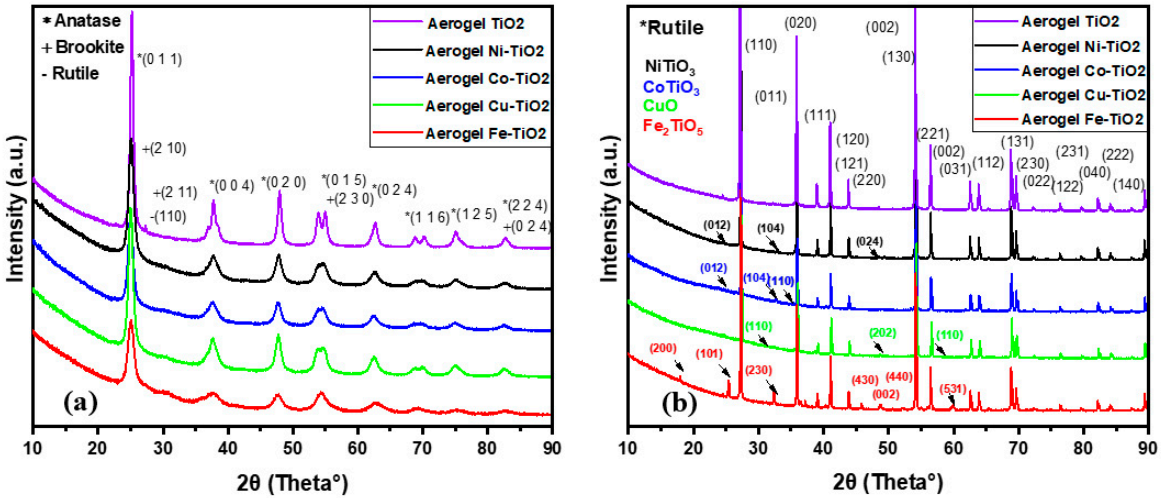


**Figure 2.** XRD patterns of metal-doped $TiO_2$ aerogels calcined at (**a**) 500 °C and (**b**) 900 °C.

**Table 1.** The phase composition and structural characteristics of the doped $TiO_2$ aerogels calcined at 500 °C and 900 °C.

| Aerogel Sample | Crystal Phases | Content of Phases (wt.%) | The Crystallite Size (nm) | Lattice Strain (%) | Lattice Parameters (nm) | | |
|---|---|---|---|---|---|---|---|
| | | | | | a | b | c |
| Temperature of calcination 500 °C | | | | | | | |
| $TiO_2$ | A | 99.08 | 11.0 | 0.4 | 0.3779 | 0.3779 | 0.9450 |
| | R | 0.92 | 8.6 | 0 | 0.4540 | 0.4540 | 0.3030 |
| Ni–$TiO_2$ | A | 75.5 | 5.0 | 0.6 | 0.3798 | 0.3798 | 0.9509 |
| | B | 24 | 2.0 | 2.3 | 0.9313 | 0.5433 | 0.5308 |
| | $NiTiO_3$ | 0.6 | 3.2 | 1.3 | 0.4367 | 0.4367 | 0.1253 |
| Co–$TiO_2$ | A | 79 | 7.1 | 0.8 | 0.3770 | 0.3770 | 0.9390 |
| | B | 20 | 2.2 | 2.5 | 0.937 | 0.5446 | 0.5357 |
| | $Co_3O_4$ | 1.0 | 2.3 | 0.52 | 0.7054 | 0.7054 | 0.7054 |
| Cu–$TiO_2$ | A | 77.2 | 7.0 | 0.4 | 0.3784 | 0.3784 | 0.9400 |
| | B | 22 | 3.0 | 1.3 | 0.907 | 0.566 | 0.5300 |
| | $Cu_3TiO_4$ | 0.8 | 5.0 | 0.74 | 0.319 | 0.319 | 0.1030 |
| Fe–$TiO_2$ | A | 82 | 4.4 | 0.4 | 0.3778 | 0.3778 | 0.9410 |
| | B | 16 | 3.0 | 1.24 | 0.9540 | 0.5582 | 0.4768 |
| | $FeTiO_3$ | 2.0 | 2.0 | 2.7 | 0.2482 | 0.9830 | 0.6180 |
| Temperature of calcination 900 °C | | | | | | | |
| $TiO_2$ | R | 100 | 66.2 | 0 | 0.4603 | 0.4603 | 0.2967 |
| Ni–$TiO_2$ | R | 98 | 72.3 | 0 | 0.4602 | 0.4602 | 0.2966 |
| | $NiTiO_3$ | 2 | 15.3 | 0.35 | 0.5036 | 0.5036 | 1.3814 |
| Co–$TiO_2$ | R | 95 | 69.0 | 0 | 0.4599 | 0.4599 | 0.29643 |
| | $CoTiO_3$ | 5 | 20.0 | 0.25 | 0.5066 | 0.5066 | 1.3928 |
| Cu–$TiO_2$ | A | 2.2 | 10.1 | 0.45 | 0.3852 | 0.3852 | 0.9806 |
| | R | 93 | 78.0 | 0 | 0.4596 | 0.4596 | 0.2962 |
| | CuO | 4.8 | 3.3 | 1.5 | 0.3884 | 0.2879 | 0.559 |
| Fe–$TiO_2$ | R | 87.3 | 67.0 | 0.01 | 0.4602 | 0.4602 | 0.2966 |
| | $Fe_2TiO_5$ | 12.7 | 36.4 | 0.14 | 0.9803 | 1.0002 | 0.3729 |

Note: the crystal phases are denoted by A (Anatase), B (Brookite), and R (Rutile).

For samples calcined at 500 °C, Ni–$TiO_2$ had the smallest crystallite size (2–5 nm), while Co–$TiO_2$ showed the largest crystallite size (2–7.1 nm). Co–$TiO_2$ showed the highest strain (0.8–2.5%). On the other hand, $TiO_2$ aerogel showed the lowest strain (0.4%), which confirms the absence of dopants and well-crystalline phases. Fe–$TiO_2$ had the most $FeTiO_3$ phase (2 wt%), while the other samples had only a small amount of the doped phase. The $TiO_2$ aerogel had the most anatase phase (99.08%), while the other samples contained a mixture of different $TiO_2$ phases, including doped ones. Overall, the samples had similar lattice parameters and crystallite sizes but differed in strain and phase with the dopants present in the aerogels.

#### 2.1.1. The Influence of Lattice Strain on the Crystalline Size and Photocatalytic Activity of Metal-Doped $TiO_2$ Aerogels

Lattice strain can affect the electronic properties of a material and its crystal structure. Therefore, it can affect its photocatalytic activity [38]. In the case of the brookite phase, the stress affected its crystal structure and caused peak broadening in the XRD patterns. Strain can come from various sources, such as vacancies, point defects, and dislocations. Brookite strain ranged from 1.24% to 2.5% for Fe–$TiO_2$ and Co–$TiO_2$ samples. The $FeTiO_3$ phase was one of the highest in contrast to that of $Co_3O_4$, which was 0.52%. Looking at Table 1, we can see that doped samples generally have smaller crystallite sizes than undoped $TiO_2$ at 500 °C. This difference may be due to the incorporation of dopant ions

that could hinder the growth of $TiO_2$ crystals. Based on the data provided, it can be seen that samples calcined at 900 °C generally have larger crystallite sizes than samples calcined at 500 °C. For example, in the Ni–$TiO_2$ aerogel, the $NiTiO_3$ phase has a larger crystallite size (3.2 ± 12 nm vs. 15.3 ± 3 nm) and a lower strain (1.3% vs. 0.35%) after calcination at 900 °C compared with 500 °C. A smaller crystal size leads to a larger surface area and better photocatalytic activity [39].

Regarding the correlation between stress and crystal size, smaller crystal sizes can result in higher stress due to the presence of defects and dislocations. Stress can hinder crystal growth, which can also affect crystal size. It follows that the stress in different crystalline phases can play a non-negligible role in the photocatalytic activity of $TiO_2$. The smaller crystal sizes of the doped samples could be the reason that contributes to their higher photocatalytic activity, apart from the doping ions themselves. The crystallite sizes determined by XRD analysis (see Table 1) are consistent with the TEM micrographs in Figure 3. These show that the particle size of the doped aerogels ranged from 2 nm to 7 nm for the samples calcined at 500 °C, with the doped Cu–$TiO_2$ aerogel having the largest nanoparticle size [14]. The observed increase in particle size may be attributed to the larger crystallite size of the dopant phase present in the Cu-$TiO_2$ aerogel in comparison with the other dopant phases from Ni, Co, and Fe.

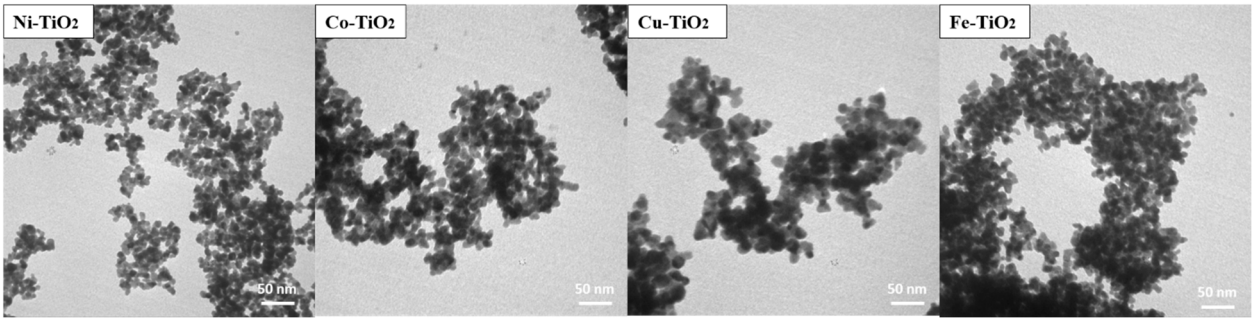


**Figure 3.** TEM images of the anatase/brookite metal-doped $TiO_2$ by Ni, Co, Cu, and Fe calcined at 500 °C.

### 2.1.2. The Role of Dopants on the Crystal Structure and Phase Composition of $TiO_2$

As can be seen in the table, the undoped $TiO_2$ sample calcined at 500 °C contains both anatase and rutile phases, which is a common composition after the transformation of part of the anatase to rutile at high temperature. In contrast, samples of doped $TiO_2$ calcined at 500 °C mainly contain anatase and brookite phases. This fact could be due to dopant ions that affected the crystal structure and growth of $TiO_2$ particles. For example, $Ni^{2+}$ ions have been reported to stabilize the anatase phase [40], while $Cu^{2+}$ and $Fe^{3+}$ ions promote the formation of the brookite phase. $Co^{2+}$ ions did not interact with $TiO_2$, resulting in a mixture of the $TiO_2$ phase and a small percentage of cobalt oxide $Co_3O_4$ [41]. $Co^{3+}$-O and $Co^{2+}$-O bonds existing in $Co_3O_4$ formed aggregates on the $TiO_2$ surface [42]. The fact that the dopant precursors were acetate salts may have contributed to stabilizing specific phases, as the acetate ions could act as chelating agents and affect crystal growth and $TiO_2$ particle formation. In addition, the presence of dopants could affect the nucleation and growth of $TiO_2$ crystals, leading to different phase compositions. In summary, the presence of dopants in the $TiO_2$ samples affected the crystal structure and phase composition, forming anatase and brookite phases rather than rutile. Dopant ions and their precursor forms may have played a role in determining the final phase composition of $TiO_2$ aerogel samples [1,43], such as $NiTiO_3$ [44,45], $CoTiO_3$, CuO, and $Fe_2TiO_5$ (pseudobrookite) [46,47]. These new phases may have different properties than the original $TiO_2$ phase and may affect the photoactivity of the samples [48].

### 2.2. Effect of Metal-Doped $TiO_2$ Aerogels on the Textural Parameters and Electronic Properties

The textural parameters of the metal-doped $TiO_2$ samples calcined at 500 °C were studied using the nitrogen adsorption/desorption isotherms shown in Figure 4a. The pore size distributions (DVP) calculated from the desorption branches of the isotherm are shown in Figure 4b. Following IUPAC [49], all samples showed similar physisorption isotherms. These are typical solids with a mesoporous network and macropores that do not contain pore condensate. The textural parameter values (BET SSA specific surface area, BJH pore size, and pore volume) are shown in Table 2. Increasing the calcination temperature from 500 °C to 900 °C caused an extreme decrease in the specific surface area (SSA) of $TiO_2$ samples doped with metal from 160 $m^2 \cdot g^{-1}$ to <5 $m^2 \cdot g^{-1}$. The mesoporous structure of the metal-doped $TiO_2$ aerogels can be seen in Figure 5 for the aerogels calcined at 500 °C and the decrease in the BET SSA value of the sintered samples at 900 °C. Sintering at a temperature of 900 °C led to an excessive reduction of the surface area of photocatalytic aerogels [3,37]. For samples calcined at 500 °C, the Fe–$TiO_2$ doped aerogel had the highest absorption volume and smaller than average pore size. The metal-doped $TiO_2$ aerogels were found to have an average pore size ranging from 12 nm to 18 nm. A $TiO_2$ aerogel sample calcined at 500 °C shows that increasing the pore size decreased the cumulative pore volume and area (Table 2) [50].

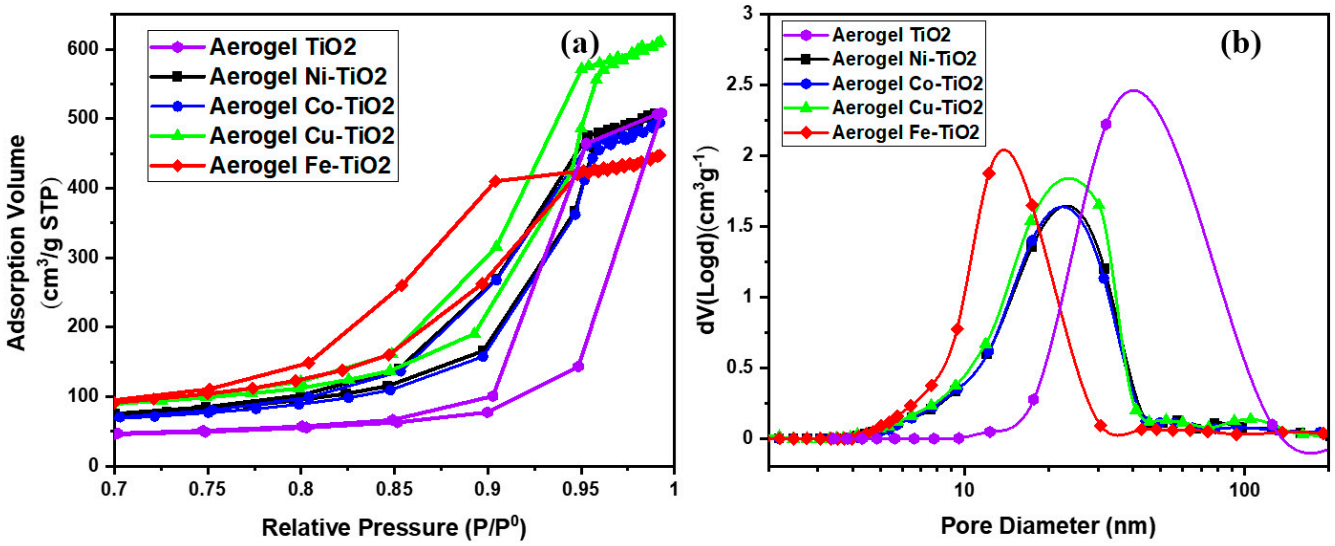


**Figure 4.** (**a**) BET–$N_2$ absorption-desorption and (**b**) BJH pore size distribution for the metal-doped aerogel samples calcined at 500 °C.

**Table 2.** Physicochemical and photocatalytic properties of the doped $TiO_2$ aerogels with Ni, Co, Cu, and Fe calcined at 500 °C.

| Material | B/A Ratio | BET SSA ($m^2 \cdot g^{-1}$) | BJH Pore Size (nm) | BJH Pore Volume ($cm^3/g^{-1}$) | Band Gap (eV) |
|---|---|---|---|---|---|
| $TiO_2$ aerogel | 0 | 86.5 | 32.1 | 0.79 | 3.0 |
| Ni–$TiO_2$ aerogel | 0.31 | 129.3 | 17.4 | 0.82 | 2.1 |
| Co–$TiO_2$ aerogel | 0.25 | 115.7 | 17.5 | 0.80 | 2.4 |
| Cu–$TiO_2$ aerogel | 0.28 | 157.6 | 17.2 | 0.98 | 2.3 |
| Fe–$TiO_2$ aerogel | 0.19 | 158.1 | 12.2 | 0.73 | 1.7 |

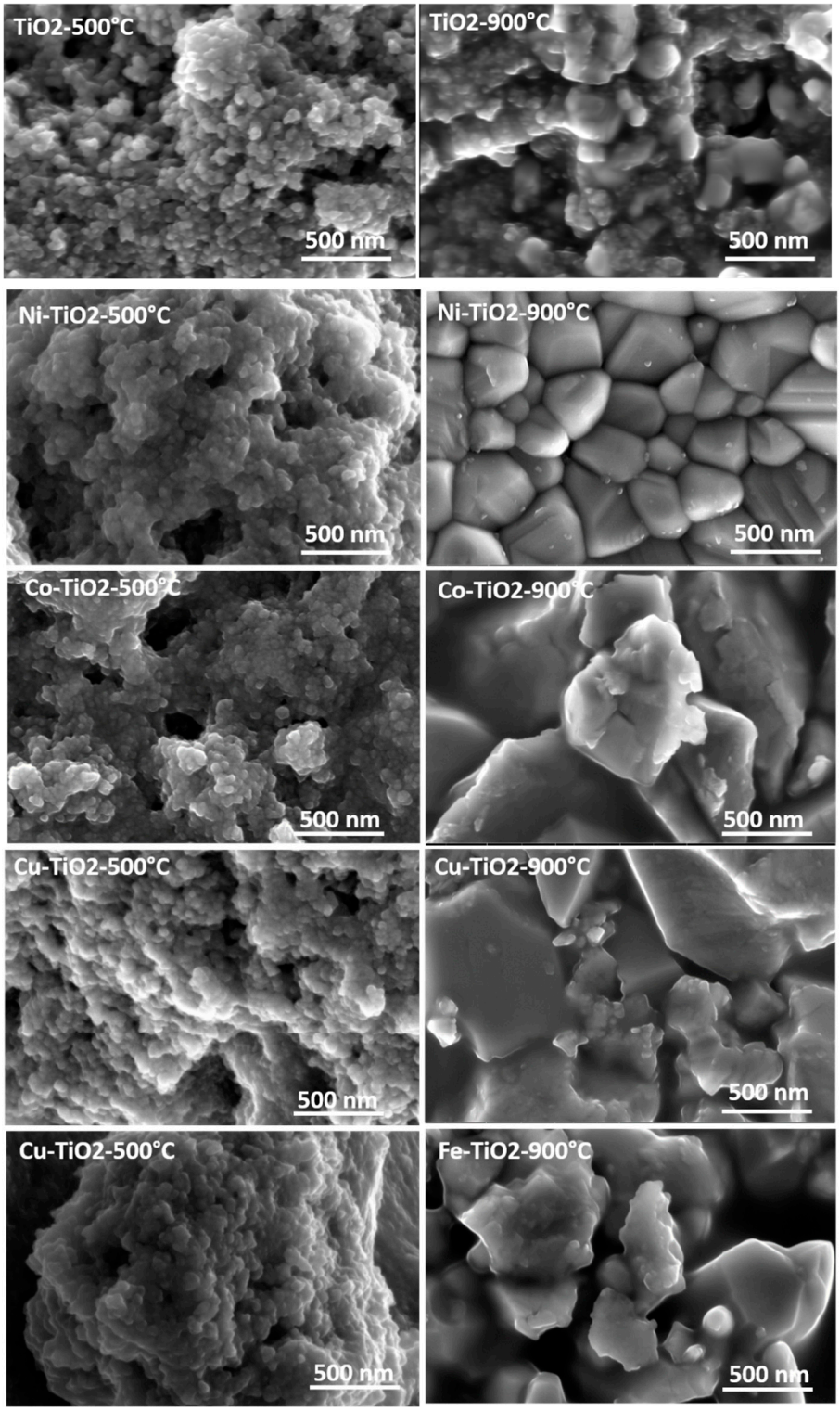


**Figure 5.** SEM images of the $TiO_2$ and metal-doped $TiO_2$ aerogels calcined at 500 °C and 900 °C.

The specific surface area of $TiO_2$ significantly affects the photocatalytic activity [51], Table 2 shows that the undoped $TiO_2$ aerogels have an SSA of 86.48 $m^2.g^{-1}$, and its value increased by doping Ni, Co, Cu, and Fe. The highest BET SSA value was observed for Fe–$TiO_2$ (158.1 $m^2 \cdot g^{-1}$), followed by Cu–$TiO_2$ (157.6 $m^2 \cdot g^{-1}$), Ni–$TiO_2$ (129.3 $m^2 \cdot g^{-1}$), and Co–$TiO_2$ (115.7 $m^2 \cdot g^{-1}$). The BJH pore size, which refers to the average pore size in the material, was 32.1 nm for the $TiO_2$ aerogel and was lower for the doped samples. The smallest pore size was observed for Fe–$TiO_2$ (12.2 nm), followed by Ni–$TiO_2$, Co–$TiO_2$,

and Cu–$TiO_2$, all with pore sizes of about 17 nm. The total pore volume in the material remained similar for Co–$TiO_2$ (0.80 $cm^3/g^{-1}$) and Ni–$TiO_2$ (0.82 $cm^3/g^{-1}$), followed by Cu–$TiO_2$ (0.98 $cm^3/g^{-1}$) [52]. The lowest pore volume value was observed for Fe–$TiO_2$ (0.73 $cm^3/g^{-1}$). Thus, the presented data showed that doping the $TiO_2$ aerogel with Ni, Co, Cu, and Fe ions significantly increased the surface area but decreased the pore size and had negligible influence on the pore volume. Among the doped samples, Cu–$TiO_2$ had the highest BET SSA and BJH pore volume, while Fe–$TiO_2$ had the smallest pore size. These physicochemical properties are fundamental factors in determining the photocatalytic activity of materials. In the case of $TiO_2$-doped aerogels, it was observed that the BET SSA decreased with increasing brookite to anatase ratio (B/A), and the pore size and pore volume also decreased.

The band gap in $TiO_2$ aerogels doped with Ni, Co, Cu, and Fe and in the undoped sample calcined at 500 °C was calculated using indirect $\alpha^{1/2}$ transitions, as shown in Figure 6. The relationship between surface area (SSA) and the size of the pores of the materials and their band gaps are presented in this work The $TiO_2$ aerogel had the largest band gap (3.0 eV), the smallest specific surface area, and the most significant pore size of all aerogels. This result is consistent with the relationship between the higher band gap and the lower surface area [52]. However, all doped aerogels have a smaller band gap than the undoped $TiO_2$ aerogel. This result is probably due to the introduction of dopant atoms that create defects, leading to the narrowing of the band gap. Table 2 shows that the Fe–$TiO_2$ aerogel has the smallest bandgap (1.7 eV) and the most significant BET SSA [21]. A similar relationship between B/A ratio, pore size, and band gap was observed for Ni–$TiO_2$, Co–$TiO_2$, and Cu–$TiO_2$, which showed similar B/A ratios, pore size, and band gap with slightly higher values than Fe–$TiO_2$.

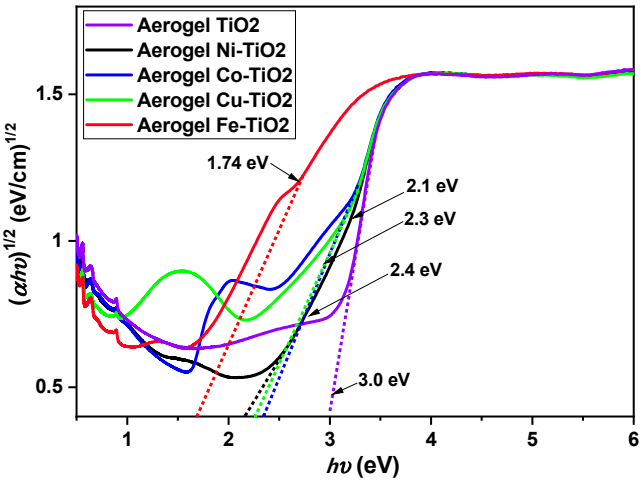


**Figure 6.** Indirect bandgap measurements of Ni-, Co-, Cu-, and Fe-doped $TiO_2$ aerogels calcined at 500 °C.

Overall, the results of this study indicate that the band gap of $TiO_2$ aerogel and doped $TiO_2$ aerogels is influenced by the presence of dopants and the material composition, surface area, and pore size, which may have implications for their photocatalytic activity.

### *2.3. Chemical Composition of the Metal-Doped $TiO_2$ Aerogels: Ni, Co, Cu, Fe*

Energy dispersive X-ray spectroscopic analysis (EDS) was used to analyze the chemical composition of the synthesized metal-doped $TiO_2$ aerogels calcined at 500 °C. Table 3 shows that $TiO_2$ doped aerogels contained 0.7 wt.% Ni, 0.7 wt.% Co, 1.9 wt.% Cu, and 4.9 wt.% Fe [52]. The doped aerogels mainly contained $TiO_2$, as evidenced by peaks associated with titanium and oxygen (Figure S2). EDS elemental maps of $TiO_2$ aerogels doped with Ni, Co, Cu, and Fe, shown in Figure 7, show a homogeneous distribution of elements without agglomeration [53].

**Table 3.** SEM–EDS elemental composition of the Ni-, Co-, Cu-, Fe-doped $TiO_2$ aerogels calcined at 500 °C.

| Element | Ti | | O | | (Ni, Co, Cu, and Fe) | |
|---|---|---|---|---|---|---|
| **Material** | **Wt.%** | **At%** | **Wt.%** | **At%** | **Wt.%** | **At%** |
| Ni–$TiO_2$ aerogel | 61.6 | 35 | 37.7 | 64.7 | 0.7 | 0.3 |
| Co–$TiO_2$ aerogel | 55.6 | 29.6 | 43.7 | 70.1 | 0.7 | 0.3 |
| Cu–$TiO_2$ aerogel | 52.2 | 27.3 | 45.9 | 72 | 1.9 | 0.7 |
| Fe–$TiO_2$ aerogel | 42.9 | 21.1 | 52.2 | 76.9 | 4.9 | 2.1 |

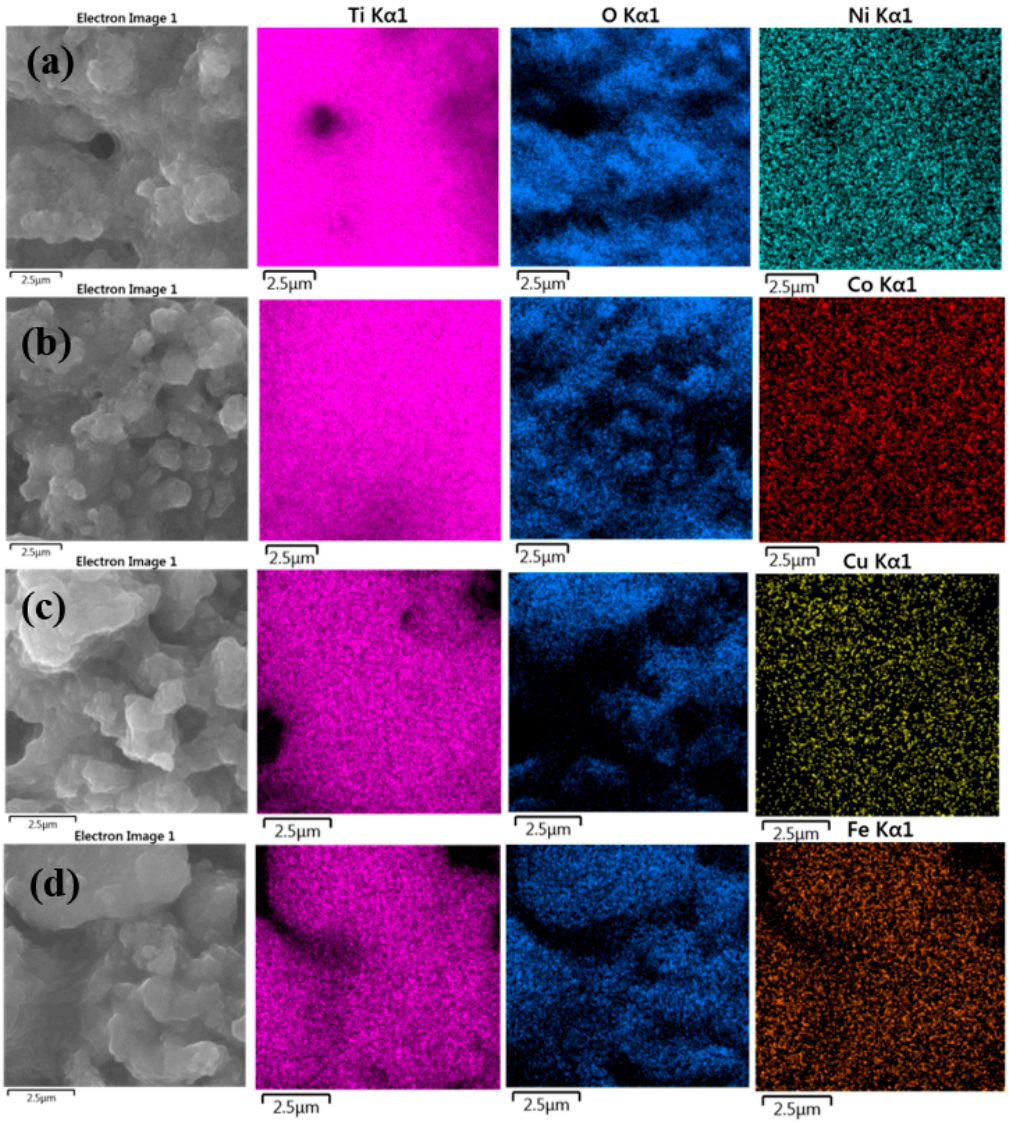


**Figure 7.** EDS chemical mapping spectra of the metal-doped $TiO_2$ aerogels (**a**) Ni, (**b**) Co, (**c**) Cu, (**d**) Fe calcined at 500 °C.

X-ray photoelectron spectroscopy (XPS) was used to analyze the elemental surface composition of metal-doped $TiO_2$ aerogels. Figure 8 shows wide, high-resolution XPS scans of Ti 2p, O 1s, and C 1s peaks, along with the additional metals Ni 2p [54], Co 2p [25], Cu 2p, and Fe 2p [55], of $TiO_2$ aerogels calcined at 500 °C. The two Ti 2p peaks in the XPS spectra are specified in Table 4 and have binding energies of 464.5 and 458.7 eV, corresponding to $Ti^{4+}$ $2p^{3/2}$ and $Ti^{4+}$ $2p^{1/2}$ [56]. The carbon content of the sample is related to the trace organic residue bound as Ti–$OCH(CH_3)_2$ [9]. Quantifications in mass

and atomic concentrations provide satisfactory fitting (Table S1) and are consistent with SEM–EDS results.

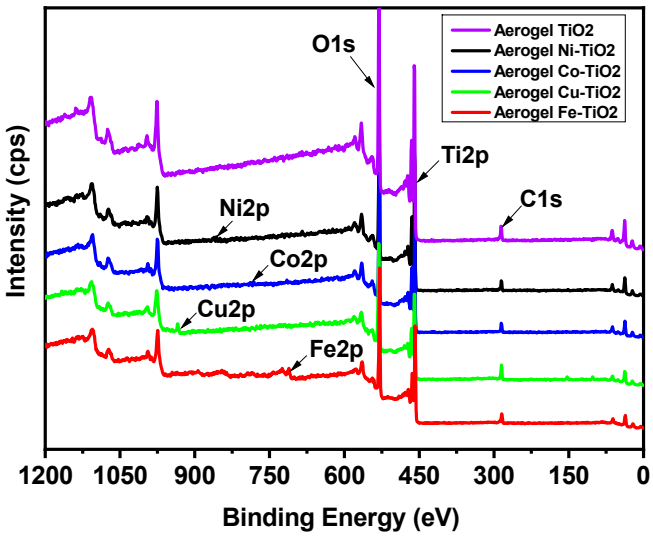


**Figure 8.** XPS chemical composition spectra of the doped $TiO_2$ aerogels by Ni, Co, Cu, and Fe calcined at 500 °C.

**Table 4.** XPS chemical composition and quantification of the doped $TiO_2$ aerogels by Ni, Co, Cu, and Fe calcined at 500 °C.

| Aerogel Samples | $TiO_2$ | | $Ni–TiO_2$ | | $Co–TiO_2$ | | $Cu–TiO_2$ | | $Fe–TiO_2$ | |
|---|---|---|---|---|---|---|---|---|---|---|
| **Elements** | **Wt.%** | **At.%** | **Wt.%** | **At.%** | **Wt.%** | **At.%** | **Wt.%** | **At.%** | **Wt.%** | **At.%** |
| C 1s (285.5 eV) | 6.70 | 13.55 | 6.45 | 13.02 | 5.78 | 11.9 | 10.3 | 19.7 | 6.95 | 13.9 |
| Ti 2p (458.7–464.5 eV) | 54.62 | 27.72 | 52.89 | 26.79 | 54.98 | 28.5 | 48.2 | 23.1 | 47.95 | 24.04 |
| O 1s (530.2 eV) | 38.67 | 58.72 | 39.37 | 59.66 | 38.09 | 59.1 | 39.24 | 56.3 | 39.9 | 59.8 |
| Ni, Co, Cu, and Fe 2p (861.4 eV, 787.2, 933.9 eV, 711.3) | - | - | 1.29 | 0.53 | 1.16 | 0.49 | 2.21 | 0.8 | 5.27 | 2.27 |

Chemical analysis (Tables 3 and 4) shows that the dopant concentration affected the surface area and physicochemical properties of the $TiO_2$ aerogel samples (Table 1). It was found that metal ion admixtures such as Cu and Fe increased the surface area of $TiO_2$ aerogel [57]. The specific metal ion used as a dopant can also affect the physicochemical properties of the material, such as band gap energy and redox properties with different oxidation states. The effect of dopant concentration also depends on the specific type of dopant used and the experimental conditions of $TiO_2$ preparation [48].

The presence of metal ions in the samples was further verified using electron paramagnetic resonance (EPR) at low temperature (77K). Figure 9a–e shows the EPR spectra of the undoped $TiO_2$ aerogel and metal-doped $TiO_2$ aerogels. $Cu^{2+}$ [13,58], $Fe^{3+}$, $Ni^{3+}$, and $Co^{2+}$ ions [25] can be seen. $TiO_2$ aerogel and metal-doped $TiO_2$ aerogels exhibit additional paramagnetic species potentially associated with forming oxygen vacancies and defects [51] with a g factor ranging from 1.99 to 2.00 [59]. The g factors obtained for $Ni^{3+}$, $Co^{2+}$, and $Cu^{2+}$ were 2.01 [60], 2.00 [61], and 2.13 [62], respectively, in agreement with the literature. $Ni^{2+}$ was partially oxidized to $Ni^{3+}$, which decreased the simultaneous broadening of the EPR signal [60]. The presence of two resonance peaks at $g = 2.00$ and at $g = 4.12$, respectively, were attributed to $Fe^{3+}$ ions substituted in the anatase $TiO_2$ structure. The study showed the presence of isolated octahedral $Fe^{3+}$ ions in anatase surrounded by $Ti^{4+}$ ions [46]. These observations can be explained by the diffusion of iron ions from the $TiO_2$ surface into the oxide lattice at $g$~2.0 and at $g$~4.0. These species are attributed to high-spin $Fe^{3+}$ ions (spin S = 5/2) in the rhombic states of the ligand field, in this case with a distorted rhombic envi-

ronment in the anatase phase, or to iron cations in the orthorhombic brookite structure [63]. The signal at $g$ = 1.99, recorded in Fe-$TiO_2$, was attributed to $Ti^{4+}$-substituted $Fe^{3+}$ ions in the $TiO_2$ lattice. The presence of $Fe^{3+}$ ions observed at $g$~2.0 with EPR suggests that the dopants are located in small iron oxide-type clusters or tiny nanoparticles within the $TiO_2$ anatase framework. Figure 10 displays STEM-EDS maps indicating the presence of $Fe^{3+}$ ions in the $TiO_2$ aerogel and Fe clusters segregated on the surface of $TiO_2$ nanoparticles. Additionally, the signal detected at $g$~4.0 was associated with the presence of oxygen vacancies caused by isolated rhombic $Fe^{3+}$ ions [46]. The EPR parameters of the $Cu^{2+}$ ion were reported in the range of $g$ = 2.05–2.10. In this range, it is assumed that oxides containing metal ions such as $Ti^{4+}$ or $Ti^{3+}$ and $Cu^{2+}$ were produced during the calcination process of the material. As a result of this process, $Cu^{2+}$ can be distributed in the $TiO_2$ ground structure [43].

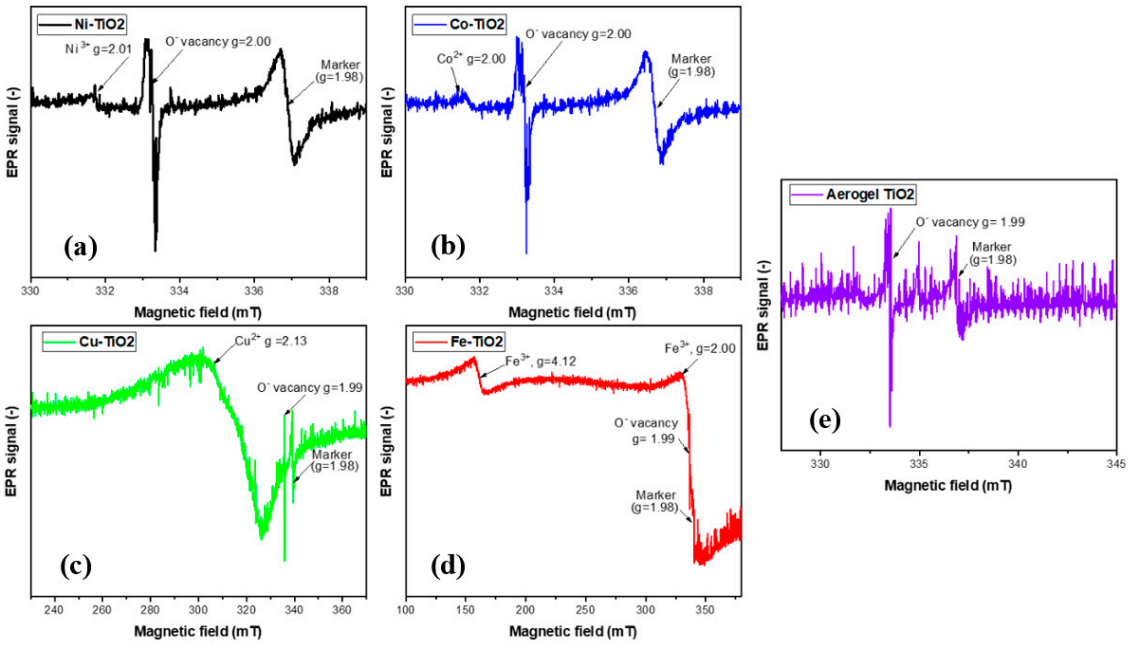


**Figure 9.** EPR spectra of (**a**) Ni-, (**b**) Co-, (**c**) Cu-, (**d**) Fe-doped $TiO_2$, (**e**) aerogels calcined at 500 °C.

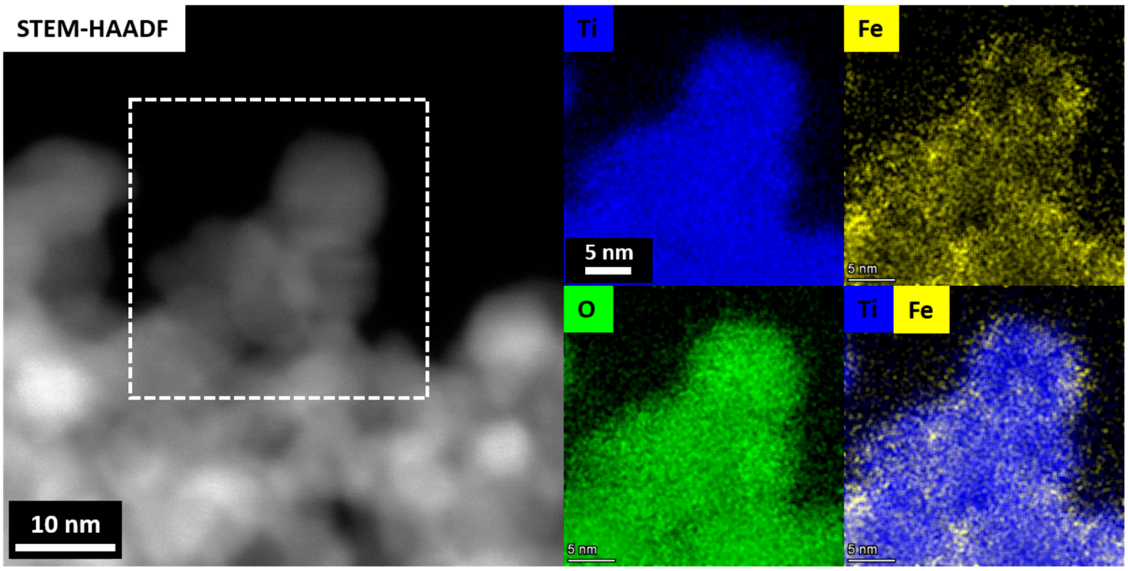


**Figure 10.** STEM–HAADF and corresponding STEM–EDS maps of the Fe–$TiO_2$ aerogel sample showing the $Fe^{3+}$ ions in the $TiO_2$ aerogel matrix and the segregated Fe phase clusters on the surface of the $TiO_2$ nanoparticles.

Figure 11 shows the FTIR spectra of metal-doped $TiO_2$ aerogels calcined at 500 °C. Ti–O–Ti, Ni–O–Ti, Co–O–Ti, Cu–O–Ti and Fe–O–Ti bonding was presented at vibrational frequencies of 500–1200 $cm^{-1}$ [55]. The band at 738 $cm^{-1}$ is attributed to stretching vibrations of the Ti–O titanium backbone. The O-H stretching vibrations of adsorbed water and the surface O-H bending group are the causes of the band of two-phase metal-doped $TiO_2$ aerogels in the region of 3200–3800 $cm^{-1}$ and in the band of 1400–1600 $cm^{-1}$, respectively. Metal-doped $TiO_2$ aerogels developed two-phase bands at 3679 and 3797 $cm^{-1}$ due to hydrogen bonding between water and carbonate anion dispersed on the surface [36]. These results are consistent with previous studies that indicated that adsorbed water could facilitate photocatalytic H–OH bond cleavage [64]. Asymmetric carboxylate segments have 1442 $cm^{-1}$ and symmetric carboxylate segments have 1689 $cm^{-1}$, corresponding to monodentate bridging in heterojunctions [9,65]. Moreover, the one at 1519.69 $cm^{-1}$ is due to the stretching band of the carbon–carbon double bond. After calcination of metal-doped two-phase $TiO_2$ aerogels at 500 °C, the carboxyl group was oxidized and cleaved in $CO_2$. This process facilitated the transformation of brookite to anatase and contributed to a slight increase in the proportion of the anatase phase in the metal-doped $TiO_2$ aerogels (Table 1). Ni–$TiO_2$ and Cu–$TiO_2$ doped aerogels showed significant intensities for Ti–O–C stretching vibrations with frequencies ranging from 948.93 to 1080.08 $cm^{-1}$ [66], followed by Fe–$TiO_2$ and Co–$TiO_2$. These results are consistent with the deconvoluted peaks and C1s binding energies obtained by XPS analysis for C–O–C bonds (see Figure S3 and Table S2).

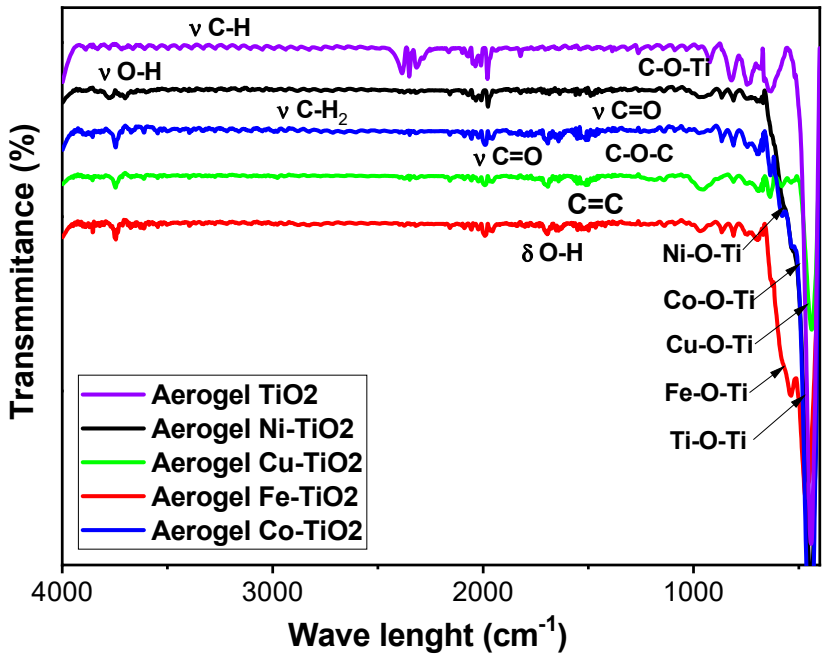


**Figure 11.** FTIR spectra of Ni-, Co-, Cu-, Fe-doped $TiO_2$ aerogels calcined at 500 °C.

The combination of different parameters, such as the brookite to anatase ratio (B/A) and the dopant composition, can affect the photocatalytic activity of the material. The nature of the dopant can also affect the physicochemical properties of the aerogel samples, such as its surface area, pore size, pore volume, and adsorption volume, which in turn can affect the material's electronic properties, such as the band gap. The band gap is an essential factor in determining the photocatalytic activity of a material because it resolves the absorbed light energy required to form electron-hole pairs. In addition, the presence of bonded ligands such as –OH and –COOH on the aerogel surface, as well as residual carbon bonded as Ti–O–C in the crystal lattice of the samples, can promote the formation of additional defects and oxygen vacancies that can serve as active sites to enhance the photocatalytic material performance [9,12,66].

### *2.4. Photoactivity of the Metal-Doped $TiO_2$ Aerogels by Ni, Co, Cu, Fe*

In order to investigate the photocatalytic activity of metal-doped $TiO_2$ aerogels calcined at 500 °C, AO7 degradation was tested. The Langmuir–Hinshelwood kinetics [67–69] was used to characterize the degradation of AO7 photocatalyzed by $TiO_2$ aerogels, which is expressed by Equation (1).

$$-dC/dt = k_{app}\, C_o \quad (1)$$

Integrating Equation (1) gives Equation (2)

$$-\ln (C/C_o) = k_{app}\, t \quad (2)$$

$C_o$ is the initial concentration, "C" is the concentration at any time "t", and "$k_{app}$" is the apparent rate constant for pseudo-first-order kinetic reaction [70,71] whose values are presented in Table 2. As shown in Figure 12a, the AO7 concentration decreased linearly with the AO7 degradation time for all metal-doped $TiO_2$ aerogels. The dependences of ln ($C/C_o$) on time are linear, presented in Figure 12b, indicating that the photocatalytic degradation of AO7 confirms the pseudo-first-order reaction kinetics.

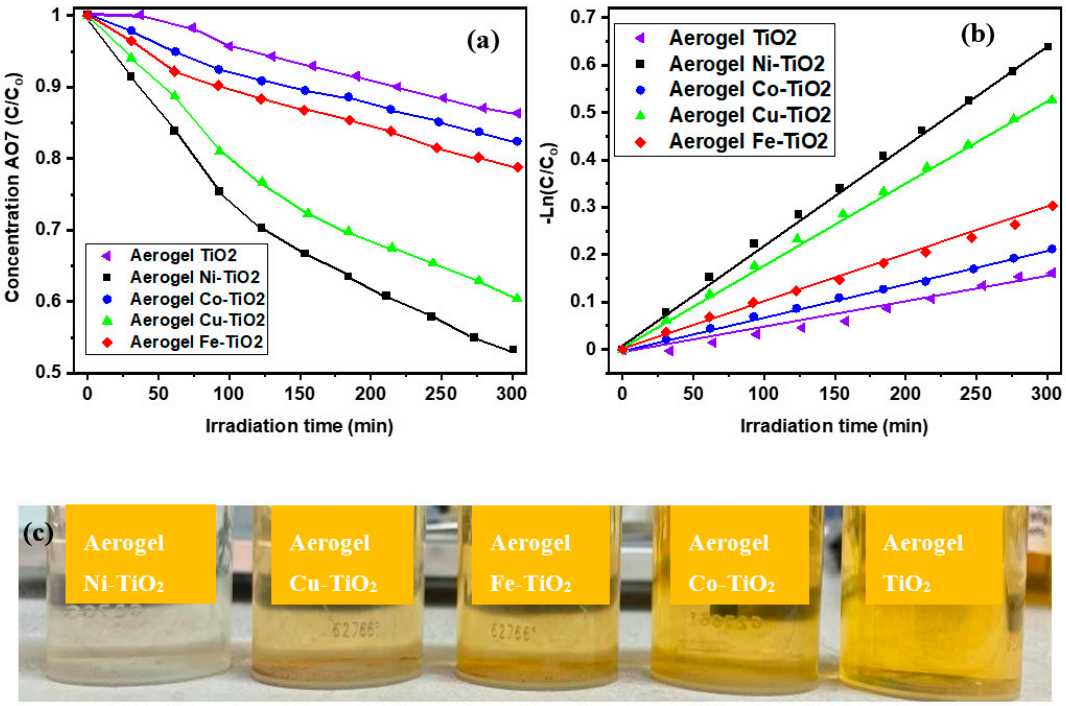


**Figure 12.** Photocatalytic performance of the Ni-, Co-, Cu-, Fe-doped $TiO_2$ aerogels: (**a**) time change of AO7 concentration during photocatalytic degradation (**b**) fitting the kinetic reaction curves ln(C/Co) = $k_{app}$ t, where $k_{app}$ refers to the apparent rate of photoactivity for the samples calcined at 500 °C, (**c**) AO7-Acid Orange 7 solution photodegradated by the metal-doped $TiO_2$ aerogels.

The highest photocatalytic activity was determined for $TiO_2$ aerogels doped with nickel ($Ni^{2+}$) and copper ($Cu^{2+}$) ions and calcined at 500 °C (Figure 12a,b). $TiO_2$ aerogels doped with cobalt ($Co^{2+}$) and iron ($Fe^{2+}$) ions had lower activity than the previous two samples (Table 5). The apparent rate constant $k_{app}$ decreased with increasing calcination temperature of doped aerogels from $2.0 \times 10^{-3}$ $min^{-1}$ (500 °C) to $1.0 \times 10^{-4}$ $min^{-1}$ (900 °C) (Figure S4). The decrease in photoactivity of the samples calcined at 900 °C was caused by the phase changes of the samples and the reduction of their specific surface area [36,54,72].

**Table 5.** Photocatalytic properties of the metal-doped $TiO_2$ aerogels by Ni, Co, Cu, F calcined at 500 °C.

| Aerogel | B/A | SSA ($m^2.g^{-1}$) | Band Gap (eV) | Dopant wt.% | $K_{app}$ ($min^{-1}$) |
|---|---|---|---|---|---|
| $TiO_2$ aerogel | 0 | 86.5 | 3.0 | 0 | $4.0 \times 10^{-4}$ |
| Ni–$TiO_2$ aerogel | 0.31 | 129.3 | 2.1 | 1.0 | $2.0 \times 10^{-3}$ |
| Co–$TiO_2$ aerogel | 0.25 | 115.7 | 2.4 | 1.0 | $6.0 \times 10^{-4}$ |
| Cu–$TiO_2$ aerogel | 0.28 | 157.6 | 2.3 | 2.0 | $1.6 \times 10^{-3}$ |
| Fe–$TiO_2$ aerogel | 0.19 | 158.1 | 1.7 | 5.0 | $7.0 \times 10^{-4}$ |

#### 2.4.1. Effect of Strain, Cristallynity, and Band Gab over Photocatalytic Performance

The strain in the $TiO_2$-doped samples could have influenced their photoactivity. Strain can affect the electronic band structure of $TiO_2$, which in turn can affect the absorption and utilization of light for the photocatalytic reaction. Based on the strain values in Table 1, the samples with the highest photoactivity, Ni–$TiO_2$ and Cu–$TiO_2$, have a relatively low strain value (0.6% and 0.4%) for the anatase phase. The doped sample with the lowest photoactivity, Co–$TiO_2$, has a higher strain value (0.8%). This finding suggests that higher strain may have reduced the photocatalytic activity of the samples, although other factors, such as crystal phase and dopant concentration, also affect the activity. This factor is evident in the Ni–$TiO_2$ sample with two crystal phases (anatase and brookite), calcined at a lower temperature (500 °C), which had higher photocatalytic activity due to a higher B/A ratio.

The band gap of the studied materials is an essential factor that affects their photocatalytic efficiency. The surface area (SSA) and pore size of a material also play a role in determining its photocatalytic activity. The Fe–$TiO_2$ aerogel form indeed has a large surface area and a suitable bandgap for photocatalytic degradation with 5 wt.% of $Fe^{3+}$ in agreement with previous reports [21], but several factors may limit its efficiency in degrading AO7. Factors that can negatively affect the photocatalytic activity of the Fe–$TiO_2$ aerogel may include less dye adsorption on the Fe–$TiO_2$ surface or the pH of the solution. AO7 has an acidic pH in the range of 3–5; at this pH, Fe–$TiO_2$ may not be fully effective. The formation of partial dopant clusters on the $TiO_2$ surface can also limit its photocatalytic activity. There are several reasons why Ni–$TiO_2$ and Cu–$TiO_2$ aerogels can be more active in the degradation of AO7 than Fe–$TiO_2$ aerogel, despite their lower surface area and smaller bandgap energy. Ni–$TiO_2$ and Cu–$TiO_2$ aerogels show higher surface electron density of states than Fe–$TiO_2$ aerogel, which may increase the photocatalytic activity by improving the separation of photo-generated electron-hole pairs [73]. The chemical structure of AO7 may be more suitable for adsorption and degradation by Ni–$TiO_2$ aerogels and Cu–$TiO_2$ than by using Fe–$TiO_2$ aerogel.

#### 2.4.2. Chemical Interaction of the Metal-Doped Aerogels during the Photodegradation of Acid Orange 7

The chemical structure of AO7 may be more suitable for degradation by Ni–$TiO_2$ and Cu–$TiO_2$ aerogels than Fe–$TiO_2$ aerogel. Some functional groups present in AO7, such as azo (–N=N–) and sulfonic acid (–$SO_3H$) groups [74], can promote the adsorption of AO7 on Ni–$TiO_2$ and Cu–$TiO_2$ aerogels more effectively than on Fe–$TiO_2$ aerogel. These functional groups can also facilitate electron transfer and increase the efficiency of the photocatalytic reaction. Ni–$TiO_2$ and Cu–$TiO_2$ can form metal–organic complexes with functional groups present in AO7. These complexes can increase the adsorption of AO7 on the surface of Ni–$TiO_2$ and Cu–$TiO_2$ aerogels and thus promote the degradation of AO7. Under UV radiation, Ni–$TiO_2$ and Cu–$TiO_2$ aerogels can be photoreduced to form NiO and CuO, which can act as $TiO_2$ cocatalysts and promote the separation of photogenerated electron-hole pairs [16,75].

2.4.3. The Impact of Dopant Concentration and Oxygen Vacancies on the Photocatalytic Efficiency of Metal-Doped Aerogel

The reason for the highest photoactivity of Ni–$TiO_2$ can be seen in Figure 13, which shows the STEM-EDS analysis of Ni–$TiO_2$. The Figure shows a homogeneous distribution of Ni in the nanostructure of the $TiO_2$ aerogel, with a concentration of 0.8 wt.% (Table S3), which is consistent with SEM–EDS and XPS analysis. A low content of Ni dopant, which did not lead to the formation of inclusions and clusters, which can act as recombination centers for photogenerated electron-hole pairs and reduce the photocatalytic activity, could have contributed to the homogeneous distribution of Ni in $TiO_2$. Oxygen vacancies can also positively affect the photocatalytic process. The presence of oxygen vacancies in the EPR spectrum of the Ni–$TiO_2$ aerogel could create surface states that act as electron traps, improving the separation of photogenerated electron-hole pairs and enhancing photocatalytic activity. It has been reported that the Ni dopant enhanced new defect states in anatase-$TiO_2$ as oxygen vacancies [29]. Oxygen vacancies can also create surface $Ti^{3+}$ species that can act as electron donors and promote the generation of reactive oxygen species (ROS) such as hydroxyl radicals (•OH), superoxide radicals ($\bullet O^{2-}$), and hydrogen peroxide ($H_2O_2$). These ROS can react with organic pollutants adsorbed on the surface of $TiO^2$ aerogels and promote their degradation [74].

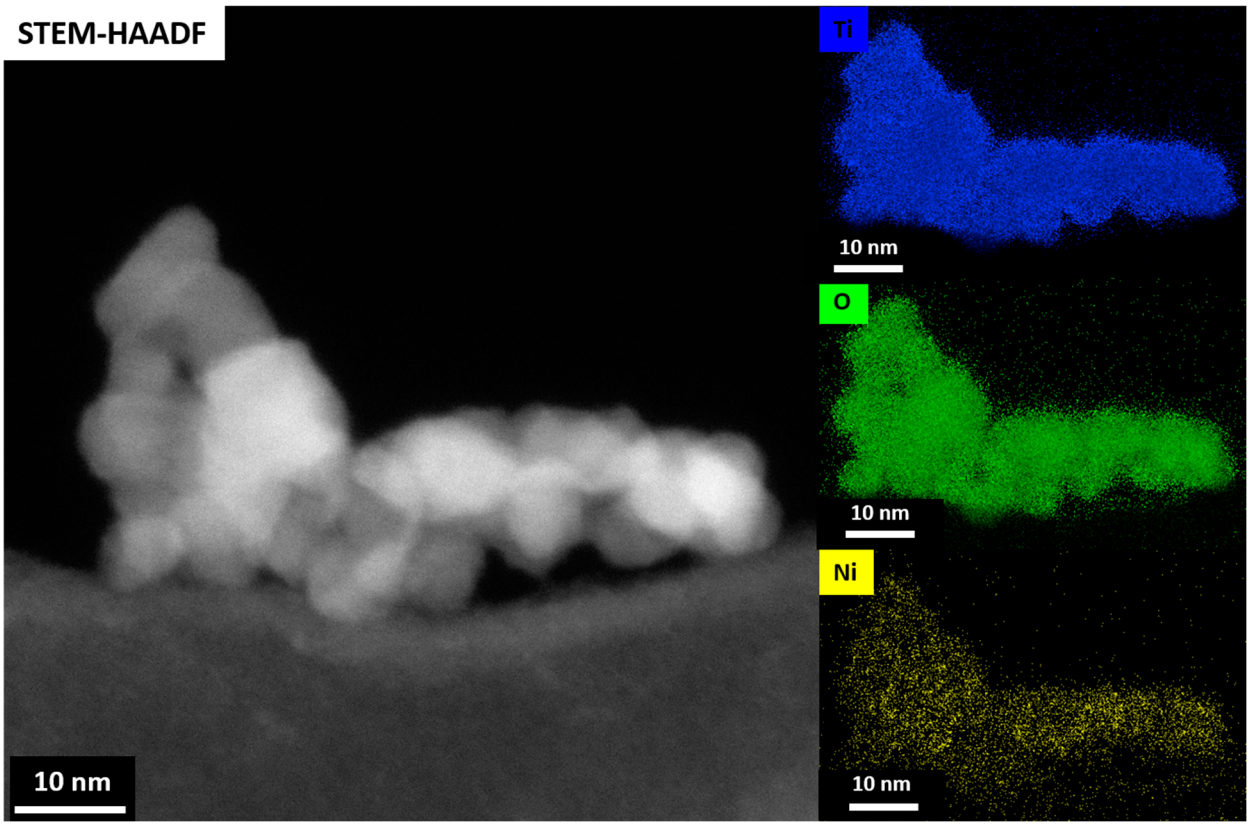


**Figure 13.** STEM–HAADF and corresponding STEM–EDS maps of the Ni–$TiO_2$ aerogel sample showing homogeneous distribution of Ni element whithin the $TiO_2$ aerogel nanoparticles and without presence of agregates from a secondary nickel phase.

## 3. Conclusions

An acid-catalyzed sol-gel process and subsequent supercritical drying prepared $TiO_2$ aerogels doped with Ni, Co, Cu and Fe. After calcination at 500 °C, the catalysts had a mesoporous structure, a significant specific surface area (SSA) ranging from 116 to 158 $m^2 \cdot g^{-1}$, a pore size of 12.2–17.5 nm, and a pore volume of 0.73–0.98 $cm^3 . g^{-1}$. EDS and XPS analysis confirmed the presence of Ni, Co, Cu, and Fe in $TiO_2$ aerogels with dopant

concentrations ranging from 1 to 5 wt.%. Doped $TiO_2$ aerogels calcined at 500 °C contained 76–82 wt.% anatase and 16–24 wt.% brookite. The crystal size of anatase was 4–7 nm, and brookite was 2–3 nm. After calcination at 900 °C, anatase and brookite transformed into rutile, the crystals became suspended, and the mesoporous structure disappeared. Metal doping affected the composition of the crystalline phases, brookite and anatase, and the formation of minor phases containing Ni, Co, Cu, or Fe.

The highest amount of brookite was found in the Ni–$TiO_2$ sample, which contained 1 wt.% Ni and had the highest photocatalytic activity in the degradation of AO7. In addition to the anatase/brookite ratio, other factors such as crystal structure and morphology, energy band gap, and surface defects influenced photocatalytic activity. The homogeneity of the distribution in the $TiO_2$ aerogels was analyzed by STEM–EDS. Seated Fe clusters on the surface of Fe–$TiO_2$ aerogel nanoparticles were the leading cause of the lowest photocatalytic activity of all doped aerogels.

Conversely, Ni–$TiO_2$ with homogeneously distributed Ni in $TiO_2$ nanoparticles had the highest photocatalytic activity. The high photocatalytic activity of Ni–$TiO_2$ and Cu–$TiO_2$ during the photodegradation of AO7 could also be supported by the formation of metal–AO7 complexes and cocatalyst effects. These interactions could enhance the photocatalytic activity of Ni–$TiO_2$ and Cu–TiO2 aerogels for AO7 degradation. The presence of oxygen vacancies in doped $TiO_2$ detected by EPR increased their photocatalytic activity by creating surface states that act as electron traps and activate the $TiO_2$ surface for better adsorption of AO7.

## 4. Materials and Methods

### *4.1. Reagents*

Nickel (II) acetate tetrahydrate ($Ni(OCOCH_3)_2$ $4H_2O$), 98%, Sigma-Aldrich (St.Louis, MO, USA), cobalt (II) acetate tetrahydrate ($(CH_3COO)_2Co{\cdot}4$ $H_2O$), p.a., Fluka, copper (II) acetate monohydrate ($(CH_3COO)_2Cu{\cdot}H_2O$), ≥98%, Sigma-Aldrich, iron (III) acetylacetonate ($Fe(C_5H_7O_2)_3$), 97%, Sigma-Aldrich, tetrapropyl orthotitanate ($(CH_3CH_2CH_2O)_4Ti$) and Tetraethyl ortho-titanate, ($(C_2H_5O)_4Ti$), 95%, Merck, for synthesis, Merck, ethanol ($CH_3CH_2OH$), 99.8%, ISO reagent, Lachner, nitric acid ($HNO_3$), Pnta, water ($H_2O$), CEITEC-demi.

### *4.2. Synthesis of the Metal-Doped $TiO_2$ Aerogels by Ni, Co, Cu, Fe*

A solution (A) with the M-acetate tetrahydrate and a solution (B) was prepared by mixing ethanol and demi water in a 250 mL beaker. The metal salt was weighed, and 7 mL of ethanol was added. Immediately, nitric acid was added. During the stirring process, the weigh-in was dissolved after 2 min. Tetrapropyl ortho-titanate was added to the reaction mixture under stirring.

The stirring speed was raised to 350 rpm, followed by dissolution after 5 min. Solution B (in one batch) was added to solution A, increasing the stirring speed to 600 rpm and mixing for 30 s. Subsequently, the reaction mixture was poured into a plastic vial for setting, resulting in fast gelation (1 min). In a couple of minutes, an adequate amount of acetone was added to the surface of the gel to avoid its evaporation, followed by its ageing/strengthening overnight. Transfer the sample into the jar with acetone was provided. The gel was allowed to continuously exchange its solvent with acetone for the next five days. Finally, the wet aged gel was dried under supercritical conditions with supercritical $CO_2$ using the medium temperature supercritical drying technique in a typical drying procedure. The autoclave is pressurized with liquid $CO_2$ to 5.8 MPa and then heated to 80 °C while maintaining a pressure of 18 MPa. With 2 bars/min of depressurization, the system slowly returns to atmospheric pressure after three hours in a supercritical state [76]. The metal-doped $TiO_2$ aerogels are obtained after cooling the autoclave to room temperature.

### 4.3. Characterization of the Metal-Doped $TiO_2$ Aerogels

X-ray powder diffraction patterns (XRD) were obtained using a Smart Lab diffractometer (Rigaku, Japan). The crystalline phases of the prepared $TiO_2$ were measured in the reflection mode (Bragg-Brentano geometry) using a Cu lamp using X-ray diffraction (XRD—Rigaku SmartLab 3 kW, Cu K$\alpha$ radiation) (Rigaku, Japan). The crystallite size and proportions of individual phases were calculated according to the Rietveld analysis and the Halder-Wagner (HW) method using the PDXL evaluation software v.3. The microstructure of the $TiO_2$ products was studied using a high-resolution scanning electron microscope 460L Verios (Thermo Fisher Scientific, Eindhoven, the Netherlands). TEM (transmission electron microscopy) LVEM 25 (Delong Ins.), provided high contrast and magnification images in the range of 15–25 Kv from the $TiO_2$ aerogels nanostructure. The specific surface area ($S_{BET}$) measurement was obtained as nitrogen physisorption isotherms at 77 K using Autosorb iQ (Quantachrome Instruments). $S_{BET}$ was calculated using five points according to the classical BET (Brunauer–Emmet–Teller) method for a $P/P_0$ range of 0.1–0.3, assuming cylindrical shape and mutually non-intersecting pores. The pore size distribution of samples was determined from adsorption and desorption isotherms between the analyzed pressures $P/P_0$ = 0.35–1.0, using the BJH (Barrett–Joyner–Halenda) method. The band gap calculation was made using the UV/Vis/NIR Spectrophotometer Jasco V-770S with a 60 mm integrating spheres with barium sulfate coating providing the reflectance measurement for solid samples with a powder sample holder, the diameter of the measuring area was 16 mm, sample thickness 0.5–6 mm and the indirect transitions allowed $\alpha^{1/2}$ method based on Kubelka–Munk function. A scanning electron microscope Mira 3 (Tescan, Shanghai, China, CZ) equipped with energy-dispersive spectroscope (Oxford Instruments, Abingdon, UK) was used for chemical composition analysis. To collect and evaluate spectra, Aztec software (OXFORD Ins, UK) was used. Additionally, a transmission electron microscopy (TEM) with a CS aberration image corrected microscope Titan Themis 60–300 Cubed (Thermo Fisher Scientific, USA) performed STEM energy dispersive X-ray (EDX) elemental mapping by using SuperX spectrometer (Thermo Fisher Scientific, Waltham, MA, USA) to reveal the presence and distribution of iron and Ni within the $TiO_2$ aerogel. EDX elemental maps were collected as a spectrum image using the Velox v.2.14 software (Thermo Fisher Scientific, USA). XPS analysis used the Axis Supra (Kratos Analytical, UK) with monochromatic K$\alpha$ radiation, 60 W emission power, magnetic lens, and the charge compensation turned on. The survey and detailed elemental spectra were measured using pass energies of 160 and 20 eV, respectively. The spectra were evaluated using the XPS Kratos ESCAPE data processing using Lorentzian–Gaussian function with a G/L ratio of 0.3. The electron paramagnetic resonance (EPR) experiments were conducted using a Magnettech X-band EPR spectrometer. The measurement was performed at 77 K using a Nitrogen Dewar Flask. The samples (weight approximately 10 mg) were prepared by locating and encapsulating them in 5 mm diameter quartz tubes with a $Cr^{4+}$ marker ($g$ = 1.98) for further $g$ factor calculation. The spectra were recorded using a microwave power of 10 mW and a modulation amplitude of 0.27 mT at 100 kHz.

### 4.4. Photoactivity Assessment of the Metal-Doped $TiO_2$ Aerogels by Using AO7 as a Model Probe Molecule

The photocatalytic test was conducted using the photoreactors under irradiation by UV–Vis light. A xenon lamp with a UV filter (03LWPG02, Barleword Scientific) was the source of radiation. The radiation wavelength range was between 250–750 nm, while the radiation intensity was 2.50 mW $cm^{-2}$. A total of 40 mL of the acid orange (AO7) water solution with an initial concentration of $1.7 \times 10^{-7}$ mol. $L^{-1}$ was magnetically stirred in a 1.5 $cm^2$ photoreactor under UV–Vis light. Next, 20 mg of the nanoparticle sample was dispersed in the solution. The UV–Vis spectrometer Red Tide USB650UV (Ocean optics) measured the photoactivity.

**Supplementary Materials:** The following supporting information can be downloaded at: https://www.mdpi.com/article/10.3390/gels9050357/s1, Figure S1: XRD spectra of the metal-doped $TiO_2$ aerogels after supercritical drying process. Figure S2: XRD spectra of the metal-doped $TiO_2$ aerogels after calcined at 500 °C. Figure S3: Deconvoluted binding energies and atomic concentrations of C 1s obtained from the primary XPS spectra from metal-doped $TiO_2$ aerogels calcined at 500 °C. Figure S4: Photocatalytic performance of the metal-doped $TiO_2$ aerogels: Ni, Co, Cu, Fe fitting the kinetic reaction curves—$\ln(C/C_o) = k_{app}\ t$, where $k_{app}$ refers to the apparent rate of photoactivity for the samples calcined at 900 °C. Table S1: Chemical quantification from the wide XPS spectra of the metal-doped $TiO_2$ aerogels. Table S2: Quantification of deconvoluted binding energies and atomic concentrations of C 1s obtained from the primary XPS spectra from metal-doped $TiO_2$ aerogels calcined at 500 °C. Table S3: STEM–EDS elemental quantification of the Ni, Ti, and O presented in the Ni–$TiO_2$ aerogel lattice after calcined at 500 °C.

**Author Contributions:** Conceptualization, C.J. and T.N.L.K.; Methodology, T.N.L.K., C.J. and B.V.; software, T.N.L.K.; validation, T.N.L.K. and K.J.; formal analysis, T.N.L.K. and K.J.; investigation, T.N.L.K. and C.J.; resources T.N.L.K., C.J. and B.V.; data curation, T.N.L.K.; writing—T.N.L.K.; writing—review and editing, T.N.L.K., C.J. and B.V.; visualization, T.N.L.K.; supervision, C.J.; project administration, C.J.; funding acquisition, C.J. All authors have read and agreed to the published version of the manuscript.

**Funding:** This work was supported by the Ministry of Education, Youth and Sports of the Czech Republic under grant no. LTC20019 and the COST Action CA18125 "Advanced Engineering and Research of Aerogels for Environment and Life Sciences" (AERoGELS), and funded by the European Commission and the CzechNanoLab Research Infrastructure supported by MEYS CR (LM2018110).

**Institutional Review Board Statement:** Not applicable.

**Informed Consent Statement:** Not applicable.

**Data Availability Statement:** Not applicable.

**Acknowledgments:** This work was conducted within the framework of the doctoral program "In Advance Material" of the Brno University of Technology, Central European Institute of Technology (CEITEC) by T.N.L.K. The authors acknowledge the support of the Ministry of Education, Youth and Sports of the Czech Republic under grant no. LTC20019. We also acknowledge CzechNanoLab Research Infrastructure supported by MEYS CR (LM2018110) and the specialists Kateřina Tmejová, Jan Michalička, Pavla Roupcová, Tkachenko Serhii, and the head of the research group, Martin Trunec. Moreover, the CEITEC MOTES lab-Magneto-Optical, THz Spectroscopy and the specialist Vinicius Tadeu Santana, as well as Delong Instruments in Brno.

**Conflicts of Interest:** The authors declare no conflict of interest.

## References

1. Hasanpour, M.; Hatami, M. Photocatalytic Performance of Aerogels for Organic Dyes Removal from Wastewaters: Review Study. *J. Mol. Liq.* **2020**, *309*, 113094. [CrossRef]
2. Kumaravel, V.; Mathew, S.; Bartlett, J.; Pillai, S.C. Photocatalytic Hydrogen Production Using Metal Doped $TiO_2$: A Review of Recent Advances. *Appl. Catal. B Environ.* **2019**, *244*, 1021–1064. [CrossRef]
3. Dorraj, M.; Goh, B.T.; Sairi, N.A.; Woi, P.M.; Basirun, W.J. Improved Visible-Light Photocatalytic Activity of $TiO_2$ Co-Doped with Copper and Iodine. *Appl. Surf. Sci.* **2018**, *439*, 999–1009. [CrossRef]
4. Khan, H.; Berk, D. Effect of a Chelating Agent on the Physicochemical Properties of $TiO_2$: Characterization and Photocatalytic Activity. *Catal. Letters* **2014**, *144*, 890–904. [CrossRef]
5. Mandari, K.K.; Police, A.K.R.; Do, J.Y.; Kang, M.; Byon, C. Rare Earth Metal Gd Influenced Defect Sites in N Doped $TiO_2$: Defect Mediated Improved Charge Transfer for Enhanced Photocatalytic Hydrogen Production. *Int. J. Hydrog. Energy* **2018**, *43*, 2073–2082. [CrossRef]
6. Cihlar, J.; Tinoco Navarro, L.K.; Kasparek, V.; Michalicka, J.; Kastyl, J.; Castkova, K.; Celko, L. Influence of LA/Ti Molar Ratio on the Complex Synthesis of Anatase/Brookite Nanoparticles and Their Hydrogen Production. *Int. J. Hydrog. Energy* **2021**, *46*, 8578–8593. [CrossRef]
7. Reza Gholipour, M.; Dinh, C.T.; Béland, F.; Do, T.O. Nanocomposite Heterojunctions as Sunlight-Driven Photocatalysts for Hydrogen Production from Water Splitting. *Nanoscale* **2015**, *7*, 8187–8208. [CrossRef]
8. Cho, H.-W.; Liao, K.-L.; Yang, J.-S.; Wu, J.-J. Revelation of Rutile Phase by Raman Scattering for Enhanced Photoelectrochemical Performance of Hydrothermally-Grown Anatase $TiO_2$ Film. *Appl. Surf. Sci.* **2018**, *440*, 125–132. [CrossRef]

9. Cihlar, J.; Navarro, L.K.T.; Cihlar, J.; Kasparek, V.; Michalicka, J.; Castkova, K.; Lazar, I.; Kastyl, J.; Celko, L.; Vesely, M.; et al. Influence of Substituted Acetic Acids on "Bridge" Synthesis of Highly Photocatalytic Active Heterophase $TiO_2$ in Hydrogen Production. *J. Sol.-Gel. Sci. Technol.* **2022**, *105*, 471–488. [CrossRef]
10. Chen, Y.; Dong, X.; Cao, Y.; Xiang, J.; Gao, H. Enhanced Photocatalytic Activities of Low-Bandgap $TiO_2$-Reduced Graphene Oxide Nanocomposites. *J. Nanoparticle Res.* **2017**, *19*, 200. [CrossRef]
11. Hippargi, G.; Mangrulkar, P.; Chilkalwar, A.; Labhsetwar, N.; Rayalu, S. Chloride Ion: A Promising Hole Scavenger for Photocatalytic Hydrogen Generation. *Int. J. Hydrog. Energy* **2018**, *43*, 6815–6823. [CrossRef]
12. Bhatkhande, D.S.; Pangarkar, V.G.; Beenackers, A.A.C.M. Photocatalytic Degradation for Environmental Applications—A Review. *J. Chem. Technol. Biotechnol.* **2002**, *77*, 102–116. [CrossRef]
13. Vargas Hernández, J.; Coste, S.; García Murillo, A.; Carrillo Romo, F.; Kassiba, A. Effects of Metal Doping (Cu, Ag, Eu) on the Electronic and Optical Behavior of Nanostructured $TiO_2$. *J. Alloys Compd.* **2017**, *710*, 355–363. [CrossRef]
14. Mathew, S.; Ganguly, P.; Rhatigan, S.; Kumaravel, V.; Byrne, C.; Hinder, S.J.; Bartlett, J.; Nolan, M.; Pillai, S.C. Cu-Doped $TiO_2$: Visible Light Assisted Photocatalytic Antimicrobial Activity. *Appl. Sci.* **2018**, *8*, 2067. [CrossRef]
15. Yasuda, M.; Matsumoto, T.; Yamashita, T. Sacrificial Hydrogen Production over $TiO_2$-Based Photocatalysts: Polyols, Carboxylic Acids, and Saccharides. *Renew. Sustain. Energy Rev.* **2018**, *81*, 1627–1635. [CrossRef]
16. Zaleska-Medynska, A.; Grabowska, E.; Marchelek, M.; Paszkiewicz-Gawron, M.; Zaleska-Medynska, A. Metal Oxide Photocatalysts. In *Metal Oxide-Based Photocatalysis*; Elsevier: Amsterdam, The Netherlands, 2018; pp. 51–209. [CrossRef]
17. Yu, Y.; Zhu, X.; Wang, L.; Wu, F.; Liu, S.; Chang, C.; Luo, X. A Simple Strategy to Design 3-Layered Au-$TiO_2$ Dual Nanoparticles Immobilized Cellulose Membranes with Enhanced Photocatalytic Activity. *Carbohydr. Polym.* **2020**, *231*, 115694. [CrossRef]
18. Cihlar, J.; Cihlar, J.; Bartonickova, E. Low-Temperature Sol-Gel Synthesis of Anatase Nanoparticles Modified by Au, Pd and Pt and Activity of $TiO_2$/Au, Pd, Pt Photocatalysts in Water Splitting. *J. Sol.-Gel. Sci. Technol.* **2013**, *65*, 430–442. [CrossRef]
19. Cihlar, J.; Vrba, R.; Castkova, K.; Cihlar, J. Effect of Transition Metal on Stability and Activity of La-Ca-M-(Al)-O (M=Co, Cr, Fe and Mn) Perovskite Oxides during Partial Oxidation of Methane. *Int. J. Hydrog. Energy* **2017**, *42*, 19920–19934. [CrossRef]
20. Moradi, V.; Jun, M.B.G.; Blackburn, A.; Herring, R.A. Significant Improvement in Visible Light Photocatalytic Activity of Fe Doped $TiO_2$ Using an Acid Treatment Process. *Appl. Surf. Sci.* **2018**, *427*, 791–799. [CrossRef]
21. Ganesh, I.; Kumar, P.P.; Gupta, A.K.; Sekhar, P.S.C.; Radha, K.; Padmanabham, G.; Sundararajan, G. Preparation and Characterization of Fe-Doped $TiO_2$ Powders for Solar Light Response and Photocatalytic Applications. *Process. Appl. Ceram.* **2012**, *6*, 21–36. [CrossRef]
22. Zaleska, A. Doped-$TiO_2$: A Review Doped-$TiO_2$: A Review. *Recent Patents Eng.* **2014**, *2*, 157–164. [CrossRef]
23. Zhang, W.; Wang, S.; Li, J.; Yang, X. Photocatalytic Hydrogen Production from Methanol Aqueous Solution under Visible-Light Using Cu/S–$TiO_2$ Prepared by Electroless Plating Method. *Catal. Commun.* **2015**, *59*, 189–194. [CrossRef]
24. Mugundan, S.; Rajamannan, B.; Viruthagiri, G.; Shanmugam, N.; Gobi, R.; Praveen, P. Synthesis and Characterization of Undoped and Cobalt-Doped TiO2 Nanoparticles via Sol–Gel Technique. *Appl. Nanosci.* **2015**, *5*, 449–456. [CrossRef]
25. Sadanandam, G.; Lalitha, K.; Kumari, V.D.; Shankar, M.V.; Subrahmanyam, M. Cobalt Doped $TiO_2$: A Stable and Efficient Photocatalyst for Continuous Hydrogen Production from Glycerol: Water Mixtures under Solar Light Irradiation. *Int. J. Hydrog. Energy* **2013**, *38*, 9655–9664. [CrossRef]
26. Seadira, T.; Sadanandam, G.; Ntho, T.A.; Lu, X.; Masuku, C.M.; Scurrell, M. Hydrogen Production from Glycerol Reforming: Conventional and Green Production. *Rev. Chem. Eng.* **2018**, *34*, 695–726. [CrossRef]
27. Franceschini, E.A.; Gomez, M.J.; Lacconi, G.I. One Step Synthesis of High Efficiency Nickel/Mesoporous TiO2 Hybrid Catalyst for Hydrogen Evolution Reaction. *J. Energy Chem.* **2019**, *29*, 79–87. [CrossRef]
28. Lamouchi, W.; Ben Slama, S.; Saadallah, F.; Bouaicha, M. Nickel Doping Induced Amorphization of Brookite $TiO_2$: Photoluminescence Enhancement. *Optik* **2021**, *227*, 166123. [CrossRef]
29. Ali, H.; Vandevyvere, T.; Lauwaert, J.; Kansal, S.K.; Saravanamurugan, S.; Thybaut, J.W. Impact of Oxygen Vacancies in Ni Supported Mixed Oxide Catalysts on Anisole Hydrodeoxygenation. *Catal. Commun.* **2022**, *164*, 106436. [CrossRef]
30. Moussaoui, R.; Elghniji, K.; ben Mosbah, M.; Elaloui, E.; Moussaoui, Y. Sol–Gel Synthesis of Highly TiO2 Aerogel Photocatalyst via High Temperature Supercritical Drying. *J. Saudi Chem. Soc.* **2017**, *21*, 751–760. [CrossRef]
31. Budtova, T.; Aguilera, D.A.; Beluns, S.; Berglund, L.; Chartier, C.; Espinosa, E.; Gaidukovs, S.; Klimek-kopyra, A.; Kmita, A.; Lachowicz, D.; et al. Biorefinery Approach for Aerogels. *Polymers* **2020**, *12*, 2779. [CrossRef] [PubMed]
32. Wang, X.; Li, C.; Shi, Z.; Zhi, M.; Hong, Z. The Investigation of an Organic Acid Assisted Sol-Gel Method for Preparing Monolithic Zirconia Aerogels. *RSC Adv.* **2018**, *8*, 8011–8020. [CrossRef] [PubMed]
33. Vorsina, I.; Grigorieva, T.; Barinova, A.; Lyakhov, N. Mechanochemical Interaction of Silicon Dioxide With Organic Acids. *Chem. Sustain. Dev.* **2011**, *19*, 236–247.
34. Cihlar, J.; Kasparek, V.; Kralova, M.; Castkova, K. Biphasic Anatase-Brookite Nanoparticles Prepared by Sol-Gel Complex Synthesis and Their Photocatalytic Activity in Hydrogen Production. *Int. J. Hydrog. Energy* **2015**, *40*, 2950–2962. [CrossRef]
35. Mahy, J.G.; Cerfontaine, V.; Poelman, D.; Devred, F.; Gaigneaux, E.M.; Heinrichs, B.; Lambert, S.D. Highly Efficient Low-Temperature N-Doped $TiO_2$ Catalysts for Visible Light Photocatalytic Applications. *Materials* **2018**, *11*, 584. [CrossRef]
36. Lal, M.; Sharma, P.; Ram, C. Calcination Temperature Effect on Titanium Oxide ($TiO_2$) Nanoparticles Synthesis. *Optik* **2021**, *241*, 166934. [CrossRef]

37. Kim, M.G.; Kang, J.M.; Lee, J.E.; Kim, K.S.; Kim, K.H.; Cho, M.; Lee, S.G. Effects of Calcination Temperature on the Phase Composition, Photocatalytic Degradation, and Virucidal Activities of $TiO_2$Nanoparticles. *ACS Omega* **2021**, *6*, 10668–10678. [CrossRef]
38. Kim, G.H.; Jeong, S. Change of Electronic Structures by Dopant-Induced Local Strain. *Sci. Rep.* **2015**, *5*, 11227. [CrossRef]
39. Zhang, A.; Zhang, Z.; Chen, J.; Sheng, W.; Sun, L.; Xiang, J. Effect of Calcination Temperature on the Activity and Structure of MnOx/$TiO_2$ Adsorbent for Hg0 Removal. *Fuel Process. Technol.* **2015**, *135*, 25–33. [CrossRef]
40. Espinos, J.P.; Gonz, A.R.; Caballero, A.; GARCfA, J.; Munuera, G. The State of Nickel in Ni/$SiO_2$ and Ni/$TiO_2$-Calcined Catalysts. *J. Catal.* **1992**, *136*, 415–422. [CrossRef]
41. Tyo, E.C.; Yin, C.; Di Vece, M.; Qian, Q.; Kwon, G.; Lee, S.; Lee, B.; Debartolo, J.E.; Seifert, S.; Winans, R.E.; et al. Oxidative Dehydrogenation of Cyclohexane on Cobalt Oxide ($Co_3O_4$) Nanoparticles: The Effect of Particle Size on Activity and Selectivity. *ACS Catal.* **2012**, *2*, 2409–2423. [CrossRef]
42. Habibi, M.H.; Shojaee, E. Synthesis of a Heterojunction $CoTiO_3$/$Co_3O_4$ Nano-Composite Thin Film with Superior Photocatalytic Activity and Reusability: Effect of Calcination Temperature on Phase Transformation and Effect of Oxidants on Enhanced Degradation of Indo Light Blue Dye. *Spectrochim. Acta—Part A Mol. Biomol. Spectrosc.* **2020**, *229*, 117796. [CrossRef] [PubMed]
43. Sakaguchi Miyamoto, N.; Miyamoto, R.; Giamello, E.; Kurisaki, T.; Wakita, H. Evaluation of Coexistent Metal Ions with $TiO_2$: An EPR Approach. *Res. Chem. Intermed.* **2018**, *44*, 4563–4575. [CrossRef]
44. Phani, A.R.; Santucci, S. Structural Characterization of Nickel Titanium Oxide Synthesized by Sol-Gel Spin Coating Technique. *Thin Solid Films* **2001**, *396*, 1–4. [CrossRef]
45. Gabal, M.A.E.F.; Al Angari, Y.M.; Obaid, A.Y. Structural Characterization and Activation Energy of $NiTiO_3$ Nanopowders Prepared by the Co-Precipitation and Impregnation with Calcinations. *Comptes Rendus Chim.* **2013**, *16*, 704–711. [CrossRef]
46. Kokorin, A.I.; Amal, R.; Teoh, W.Y.; Kulak, A.I. Studies of Nanosized Iron-Doped $TiO_2$ Photocatalysts by Spectroscopic Methods. *Appl. Magn. Reson.* **2017**, *48*, 447–459. [CrossRef]
47. Fernando, N.; Swaminathan, J.; Robles Hernandez, F.C.; Priyadarshana, G.; Sandaruwan, C.; Yang, W.; Karunaratne, V.; Wang, Z.; Amaratunga, G.A.J.; Kottegoda, N.; et al. Pseudobrookite Based Heterostructures for Efficient Electrocatalytic Hydrogen Evolution. *Mater. Rep. Energy* **2021**, *1*, 100020. [CrossRef]
48. Dubey, R.S.; Jadkar, S.R.; Bhorde, A.B. Synthesis and Characterization of Various Doped $TiO_2$ Nanocrystals for Dye-Sensitized Solar Cells. *ACS Omega* **2021**, *6*, 3470–3482. [CrossRef]
49. Rouquerol, J.; Rouquerol, F.; Llewellyn, P.; Maurin, G.; Sing, K.S.W. Adsorption by Powders and Porous Solids: Principles, Methodology and Applications. Available online: https://books.google.cz/books?hl=es&lr=&id=UOE-ZscCYncC&oi=fnd&pg=PP1&ots=0T__DEslnv&sig=jF4A7rVRX5_aDPQtMEamWcE7XvM&redir_esc=y#v=onepage&q&f=false (accessed on 9 November 2022).
50. Yu, J.; Yu, H.; Cheng, B.; Trapalis, C. Effects of Calcination Temperature on the Microstructures and Photocatalytic Activity of Titanate Nanotubes. *J. Mol. Catal. A Chem.* **2006**, *249*, 135–142. [CrossRef]
51. Wu, S.; Ishisone, K.; Sheng, Y.; Manuputty, M.Y.; Kraft, M.; Xu, R. $TiO_2$ with Controllable Oxygen Vacancies for Efficient Isopropanol Degradation: Photoactivity and Reaction Mechanism. *Catal. Sci. Technol.* **2021**, *11*, 4060–4071. [CrossRef]
52. Singh, R.; Dutta, S. Synthesis and Characterization of Solar Photoactive $TiO_2$ Nanoparticles with Enhanced Structural and Optical Properties. *Adv. Powder Technol.* **2018**, *29*, 211–219. [CrossRef]
53. Rahul, T.K.; Mohan, M.; Sandhyarani, N. Enhanced Solar Hydrogen Evolution over in Situ Gold-Platinum Bimetallic Nanoparticle-Loaded $Ti^{3+}$ Self-Doped Titania Photocatalysts. *ACS Sustain. Chem. Eng.* **2018**, *6*, 3049–3059. [CrossRef]
54. Qiu, C.; Lin, J.; Shen, J.; Liu, D.; Zhang, Z.; Lin, H.; Wang, X. Regulation of the Rutile/Anatase $TiO_2$ heterophase Interface by Ni12P5to Improve Photocatalytic Hydrogen Evolution. *Catal. Sci. Technol.* **2020**, *10*, 3709–3719. [CrossRef]
55. Liu, J.; Hodes, G.; Yan, J.; Liu, S. (Frank) Metal-Doped $Mo_2C$ (Metal = Fe, Co, Ni, Cu) as Catalysts on $TiO_2$ for Photocatalytic Hydrogen Evolution in Neutral Solution. *Chinese J. Catal.* **2020**, *42*, 205–216. [CrossRef]
56. Bharti, B.; Kumar, S.; Lee, H.N.; Kumar, R. Formation of Oxygen Vacancies and $Ti^{3+}$ State in $TiO_2$ Thin Film and Enhanced Optical Properties by Air Plasma Treatment. *Sci. Rep.* **2016**, *6*, srep32355. [CrossRef] [PubMed]
57. Lyson-Sypien, B.; Czapla, A.; Zakrzewska, K.; Swierczek, K.; Radecka, M.; Rekas, M.; Michalow, K.; Graule, T. Influence of Grain Size on Gas Sensing Properties of $TiO_2$ Nanopowders. *Procedia Eng.* **2012**, *47*, 1057–1060. [CrossRef]
58. Godiksen, A.; Stappen, F.N.; Vennestrøm, P.N.R.; Giordanino, F.; Birk Rasmussen, S.; Lundegaard, L.F.; Mossin, S.; Topsøe, H.A. Coordination Environment of Copper Sites in Cu-CHA Zeolite Investigated by Electron Paramagnetic Resonance. *J. Phys. Chem. C* **2014**, *118*, 23126–23138. [CrossRef]
59. Zhou, S.; Cižmár, E.; Potzger, K.; Krause, M.; Talut, G.; Helm, M.; Fassbender, J.; Zvyagin, S.A.; Wosnitza, J.; Schmidt, H. Origin of Magnetic Moments in Defective $TiO_2$ Single Crystals. *Phys. Rev. B* **2009**, *79*, 113201. [CrossRef]
60. Niemöller, A.; Jakes, P.; Eurich, S.; Paulus, A.; Kungl, H.; Eichel, R.-A.; Granwehr, J.; Niemöller, N.; Eichel, R.-A. Monitoring Local Redox Processes in $LiNi_{0.5}Mn_{1.5}O_4$ Battery Cathode Material by in Operando EPR Spectroscopy. *Cit. J. Chem. Phys.* **2018**, *148*, 14705. [CrossRef]
61. Savoyant, A.; Alnoor, H.; Bertaina, S.; Nur, O.; Willander, M. EPR Investigation of Pure and Co-Doped ZnO Oriented Nanocrystals. *Nanotechnology* **2017**, *28*, 035705. [CrossRef]
62. Bennett, B.; Kowalski, J.M. EPR Methods for Biological Cu(II): L-Band CW and NARS. *Methods Enzymol.* **2015**, *563*, 341. [CrossRef]

63. Kumar, C.P.; Gopal, N.O.; Wang, T.C.; Wong, M.S.; Ke, S.C. EPR Investigation of $TiO_2$ Nanoparticles with Temperature-Dependent Properties. *J. Phys. Chem. B* **2006**, *110*, 5223–5229. [CrossRef] [PubMed]
64. Khan, Z.; Shahwar, D.; Khatoon, B. Trans-Generational Response of $TiO_2$ Nanoparticles in Inducing Variability and Changes in Biochemical Pool of Lentil F2 Progenies. *J. Biosci.* **2022**, *47*, 35. [CrossRef] [PubMed]
65. Mahmoud, H.A.; Narasimharao, K.; Ali, T.T.; Khalil, K.M.S. Acidic Peptizing Agent Effect on Anatase-Rutile Ratio and Photocatalytic Performance of $TiO_2$ Nanoparticles. *Nanoscale Res. Lett.* **2018**, *13*, 48. [CrossRef] [PubMed]
66. Chelbi, S.; Djouadi, D.; Chelouche, A.; Hammiche, L.; Touam, T.; Doghmane, A. Effects of Ti-Precursor Concentration and Annealing Temperature on Structural and Morphological Properties of $TiO_2$ Nano-Aerogels Synthesized in Supercritical Ethanol. *SN Appl. Sci.* **2020**, *2*, 872. [CrossRef]
67. Asenjo, N.G.; Santamaría, R.; Blanco, C.; Granda, M.; Álvarez, P.; Menéndez, R. Correct Use of the Langmuir–Hinshelwood Equation for Proving the Absence of a Synergy Effect in the Photocatalytic Degradation of Phenol on a Suspended Mixture of Titania and Activated Carbon. *Carbon* **2013**, *55*, 62–69. [CrossRef]
68. Qourzal, S.; Barka, N.; Tamimi, M.; Assabbane, A.; Ait-Ichou, Y. Photodegradation of 2-Naphthol in Water by Artificial Light Illumination Using $TiO_2$ Photocatalyst: Identification of Intermediates and the Reaction Pathway. *Appl. Catal. A Gen.* **2008**, *334*, 386–393. [CrossRef]
69. Khan, M.M.; Ansari, S.A.; Pradhan, D.; Ansari, M.O.; Han, D.H.; Lee, J.; Cho, M.H. Band Gap Engineered $TiO_2$ Nanoparticles for Visible Light Induced Photoelectrochemical and Photocatalytic Studies. *J. Mater. Chem. A* **2014**, *2*, 637–644. [CrossRef]
70. Jafarikojour, M.; Dabir, B.; Sohrabi, M.; Royaee, S.J. Evaluation and Optimization of a New Design Photocatalytic Reactor Using Impinging Jet Stream on a $TiO_2$ Coated Disc. *Chem. Eng. Process. Process. Intensif.* **2017**, *121*, 215–223. [CrossRef]
71. Phromma, S.; Wutikhun, T.; Kasamechonchung, P.; Eksangsri, T.; Sapcharoenkun, C. Effect of Calcination Temperature on Photocatalytic Activity of Synthesized $TiO_2$ Nanoparticles via Wet Ball Milling Sol-Gel Method. *Appl. Sci.* **2020**, *10*, 993. [CrossRef]
72. Muthee, D.K.; Dejene, B.F. Effect of Annealing Temperature on Structural, Optical, and Photocatalytic Properties of Titanium Dioxide Nanoparticles. *Heliyon* **2021**, *7*, e07269. [CrossRef]
73. Ganesh, I.; Gupta, A.K.; Kumar, P.P.; Sekhar, P.S.C.; Radha, K.; Padmanabham, G.; Sundararajan, G. Preparation and Characterization of Ni-Doped $TiO_2$ Materials for Photocurrent and Photocatalytic Applications. *Sci. World J.* **2012**, *2012*, 16. [CrossRef] [PubMed]
74. Zhang, X.; Sun, D.D.; Li, G.; Wang, Y. Investigation of the Roles of Active Oxygen Species in Photodegradation of Azo Dye AO7 in $TiO_2$ Photocatalysis Illuminated by Microwave Electrodeless Lamp. *J. Photochem. Photobiol. A Chem.* **2008**, *199*, 311–315. [CrossRef]
75. Meng, A.; Zhang, L.; Cheng, B.; Yu, J. Dual Cocatalysts in $TiO_2$ Photocatalysis. *Adv. Mater.* **2019**, *31*, e1807660. [CrossRef] [PubMed]
76. Torres-Rodríguez, J.; Kalmár, J.; Menelaou, M.; Čelko, L.; Dvořak, K.; Cihlář, J.; Cihlař, J.; Kaiser, J.; Győri, E.; Veres, P.; et al. Heat Treatment Induced Phase Transformations in Zirconia and Yttria-Stabilized Zirconia Monolithic Aerogels. *J. Supercrit. Fluids* **2019**, *149*, 54–63. [CrossRef]